



University of
Massachusetts
Amherst

Bar-induced Evolution Of Dark Matter Cusps

Item Type	Article
Authors	Holley-Bockelmann, K;Weinberg, M;Katz, N
DOI	10.1111/j.1365-2966.2005.09501.x
Download date	2026-06-17 13:07:02
Link to Item	https://hdl.handle.net/20.500.14394/3142

Bar-Induced Evolution of Dark Matter Cusps

Kelly Holley-Bockelmann, Martin D. Weinberg, and Neal Katz¹

ABSTRACT

The evolution of a stellar bar transforms not only the galactic disk, but also the host dark matter halo. We present high resolution, fully self-consistent N-body simulations that clearly demonstrate that dark matter halo central density cusps flatten as the bar torques the halo. This effect is independent of the bar formation mode and occurs even for rather short bars. The halo and bar evolution is mediated by resonant interactions between orbits in the halo and the bar pattern speed, as predicted by linear Hamiltonian perturbation theory. The bar lengthens and slows as it loses angular momentum, a process that occurs even in rather warm disks. We demonstrate that the bar and halo response can be critically underestimated for experiments that are unable to resolve the relevant resonant dynamics; this occurs when the phase space in the resonant region is under sampled or plagued by noise.

Subject headings: galaxies: spiral, galaxies: kinematics and dynamics, galaxies: structure, methods: n-body simulations

1. Introduction

It is widely accepted that a galactic bar will trigger a rearrangement of the stellar and gaseous disk, but the bar's effect on the dark halo is more controversial. Linear Hamiltonian perturbation theory suggests that the transfer of angular momentum drives post-formation galaxy evolution, and is mediated by orbits that are in resonance with quasi-periodic perturbers. In the case of a barred galaxy, substantial amounts of angular momentum are transferred from the bar to the halo via resonant interactions between the bar pattern speed and the orbits of dark matter particles in the inner halo (Lynden-Bell & Kalnajs 1972, Tremaine & Weinberg 1984, Athanassoula 2000). The bar is a huge, organized source of angular momentum, and the transfer of this angular momentum from the bar to the disk-halo system causes the galaxy to evolve. The coupling between the bar and halo, and the subsequent evolution of both components, in particular the central dark matter density profile, has been conclusively shown in idealized nu-

merical experiments (Weinberg & Katz 2002, hereafter Paper I, Weinberg & Katz 2003, hereafter Paper II).

Unfortunately, attempts to study bar-halo interactions using fully self-consistent N-body simulations have lead to wildly different conclusions. For example, one robust prediction of this mechanism is that the bar pattern speed slows as it loses angular momentum to the halo, if the bar moment of inertia remains constant (Tremaine & Weinberg 1984, Weinberg 1985). While the bar does appear to slow in most N-body simulations (Athanassoula 2000, Hernquist & Weinberg 1992, Sellwood 2002, Debattista & Sellwood 2000), in others it does not (Valenzuela & Klypin 2002, hereafter VK). The discrepancy could be caused by differences in the numerical techniques, some of which might be incapable of following the important physical processes, or to differences in the disk and halo models. These could affect either the transfer of angular momentum from the bar to the halo, the evolution of the bar moment of inertia, or both.

Even for simulations that produce a slowing bar, the effect on the dark matter halo remains a point of contention. We have argued that resonant coupling between the bar and halo can flatten

¹Department of Astronomy, University of Massachusetts, Amherst, MA 01003
kelly@shrike.astro.umass.edu, weinberg@astro.umass.edu, nsk@astro.umass.edu

central dark matter density cusps (Hernquist & Weinberg 1992, Paper I, Paper II). The inner halo orbits gain enough angular momentum to move them to larger time-averaged radii, which slowly removes the central density cusp. This causes the center to lose gravitational support and accelerates the flattening. However, these results rely on idealized N-body simulations, and to date there has been only one fully self-consistent simulation that has explicitly shown the decrease in the halo central density due to this process. Such evolution can be seen in Figures 8 and 12 of Athanassoula (2003) although not mentioned in the text, but other published simulations show that the central density either remains unchanged (VK) or increases (Sellwood 2002). This has led many dynamicists to incorrectly conclude that resonant interactions are unimportant in realistic galaxy evolution, even though resonant dynamics has been shown to be crucial for bar formation (Athanassoula 2002).

Clearly, one needs to verify the predictions of linear Hamiltonian perturbation theory and those of idealized N-body simulations using realistic, high-resolution, fully self-consistent N-body simulations. This paper is one in a series designed to study bar-induced halo evolution using realistic initial conditions and a state-of-the-art N-body code that minimizes small scale noise and fully resolves the galaxy disk. Paper I (Weinberg & Katz 2002) applied the concept of bar-halo interactions to the evolution of the halo density profile using idealized N-body simulations. Paper II (Weinberg & Katz 2003) deals with common misconceptions about resonant dynamics and conducts experiments to show that the predictions of linear Hamiltonian perturbation theory pertain to idealized rigid bar and halo simulations. In this work (Paper III), we attack the fully self-consistent problem and demonstrate that resonant dynamics still applies to this regime. We show that resonant interactions between the bar pattern speed and orbits in the halo are critical to the evolution of a fully self-consistent N-body experiment.

Our fiducial simulation has a bar length of about one disk scale length. This bar length is comparable to those of recent bar-formation simulations (VK, Sellwood 2002, Athanassoula 2003). Using our low noise N-body approach, we

hope to better understand the large differences among published self-consistent N-body simulations. While it is difficult to definitively determine the cause of the differences without direct access to either their initial conditions or numerical codes, we argue that where differences exist, they are attributable to subtle numerical artifacts that destroy the important resonant dynamical processes. These processes are well described by linear perturbation theory, but the effect can be underestimated either by compromising the resonant potential through numerical noise, by having insufficient phase space coverage near the resonance, or by artificially scattering the resonant orbit reservoir. We address the problems inherent to using any N-body technique to track resonant dynamics in general, and discuss the probable shortcomings of a few recent self-consistent simulations in the discussion section.

Correctly following the physics on the ‘microscopic’ level of an individual orbit response can have effects on a galactic scale with cosmological implications. Cold dark matter (CDM) halos in every mass regime are thought to form with a characteristic density profile, expressed as $\rho(r) \propto r^{-\gamma}(1+r/r_s)^{\gamma-3}$ (Navarro et al 1997, hereafter NFW). While disagreements remain on the precise value of the central slope, γ , which range between -1 and -1.5 (Moore et al 1998, Power et al 2002), there is a consensus that primordial dark matter halos are universally cuspy. This prediction is testable using the rotation curves of galaxies. By determining the radial portion of the gravitational potential, rotation curves when combined with light profiles can constrain both luminous and dark matter density profiles. Though this technique suffers from degeneracies in interpretation, many real dark matter halos appear to be much less cuspy than those predicted by standard CDM (de Blok et. al. 2001, McGaugh 2000, Swaters et. al. 2002), and some are even consistent with a flat central profile, or density ‘core’.

If the resonant dynamic processes described above occur in real galaxies and if bars are a ubiquitous phase of early galaxy evolution, the cusp-core controversy could be reconciled through subsequent bar-halo interactions. In this scenario, primordial disks form in a cuspy dark matter halo. This proto-galactic disk is dynamically cold, making it very susceptible to bar formation. Such

young galaxies are subject to repeated satellite encounters (Tóth & Ostriker 1992, Steinmetz & Navarro 2002), and the first substantial one will likely excite a large bar in the disk (Binney & Tremaine 1987, Walker, Mihos & Hernquist 1996). The length of the bar will depend on the mass and distance of the satellite, i.e. the torque applied by an external quadrupole. The typical bar induced by this process will be much larger than those formed through internal disk instabilities, perhaps even encompassing the entire disk. The number of halo orbits commensurate with the bar pattern speed increases as the bar size increases; for a massive primordial bar, the reservoir of resonant halo orbits stretches from deep inside the halo cusp to well outside the disk, allowing a broad range of radii to accept angular momentum via resonant exchange. In idealized calculations, the torque from a primordial bar can destroy an NFW cusp out to as much as half the bar radius (Paper I, Paper II).

In this paper we emphasize moderate strength, scale-length-sized bars, so our results set a *lower limit* to the halo evolution that would be induced by tidal encounters in proto-disks. Present-day galaxies have smaller, weaker bars than those studied here and hence the present-day effects could be smaller. However, Sellwood (2002) argues that both at high and low red shift, bar sizes are restricted to the rising part of the rotation curve; this limits bar sizes to be less than a disk scale length, thus invalidating the primordial scenario outlined above. We explicitly demonstrate that this is not true if the bars are triggered externally by forming a long lived bar over four disk scale lengths in size. In addition, Athanassoula (2003) also forms bars of this size without having to resort to external triggers. Furthermore, Jogee et al (2002) show that the lengths of even local bars are severely underestimated, and can extend to beyond the disk scale length. Therefore, the scenario we outlined above remains a valid one.

We find that a bar with sizes of a disk scale length *can* remove dark matter cusps out to nearly $1/3$ of the initial disk scale length using simulations with 5 million equal mass dark matter halo particles within the virial radius. The orbits in the central regions of the halo gain enough angular momentum to remove the cusp. We demonstrate the robustness of this result by obtaining

the same result with a simulation that uses 10 million particles. Furthermore, in agreement with the predictions of linear Hamiltonian perturbation theory, both these fully self-consistent simulations show that low-order resonances are responsible for the transfer of angular momentum from the bar to the halo. We explicitly show that the angular momentum is deposited at discrete resonances in phase space, which counters some claims that resonant dynamics is only important in idealized situations. For our self-consistent field (SCF) code, we find that simulations using only 1 million particles have insufficient phase space resolution (Paper II) and too much discreteness noise to resolve the important resonances, and hence cannot follow the relevant bar-halo physics correctly. The required number of particles may be even higher for other numerical N-body techniques, which have more small scale noise. Interactions with satellites and more distant group members can also drive resonant angular momentum exchange, but are more complicated since they involve more disparate time scales. It is likely that such simulations would require many more particles than the simple bar perturbation case studied here.

We organize this paper as follows. §1 describes the models, §2 reviews the important physical processes, §3 outlines our N-body technique, how we realize our initial conditions and the specific set of experiments we perform. We present our results in §4, where we describe the bulk changes to the system, discuss the angular momentum exchange, identify the resonant interactions responsible for the halo evolution, and discuss the effect on the both the halo and disk density profiles. §5 investigates whether our results are effected by numerical artifacts: we confirm that the system is stable against centering instabilities, explore the effect of the bar formation mechanism, and discuss the effect of particle number. We present the implications of our results in §6, where we detail to what extent our final evolved halos resemble observed galaxies, and discuss the reasons for any disagreements with past work. §7 summarizes and outlines future work.

2. Physical motivation

Here we outline the physical processes and numerical considerations important to the study of

bar interactions. A much more detailed discussion can be found in §2 of Paper II. In a near-equilibrium galaxy, a global and lasting change in any conserved quantity can only occur at resonances, integer commensurabilities between orbital frequencies and a perturbation frequency. A bar is a natural rotating disturbance that resonantly exchanges angular momentum with both halo and disk orbits. To an observer sitting on the bar, these commensurate orbits describe closed, non-axisymmetric figures. Because the figures are non-axisymmetric, they will be torqued by the bar. Orbits that are slowly precessing in the bar frame, on either side of the commensurability, can also receive a torque for a finite time. But no matter how slowly an orbit precesses, if one waits long enough in a fixed potential with a constant bar pattern speed, the slow precession of the orbit eventually will describe an axisymmetric figure and would produce zero net torque. However, this time will be longer than times of interest in galaxy evolution, so in a practical sense, many orbits will be torqued. In addition, the bar pattern speed and gravitational potential are slowly evolving and, therefore, a precessing orbit may become closed and begin precessing in the opposite direction in response to this slow change. Such an orbit has *passed through the resonance*. At the point that the orbit is closed, adiabatic invariance is broken and the orbit is sensitive to the gravitational attraction of the bar through the potential associated with the resonance. Only those orbits that pass through the resonance irreversibly change their actions. The galaxy equilibrium as a whole then slowly evolves owing to these changes, and this brings fresh orbits through the resonance to continue the evolution.

The fractional change in the angular momentum of an individual orbit is antisymmetric about location of the resonance. Unless there is a gradient in phase space, as the resonance sweeps through the system orbits will pass through the resonance in both directions, and the sum of these individual changes over the ensemble of orbits containing the resonance will cancel (e.g. Weinberg 2001). A phase space gradient causes an incomplete cancellation that gives rise to a net torque. The total angular momentum gains and losses at a given time for individual orbits are first order in the bar amplitude, while the net change in the

halo’s angular momentum is second order and results from the near cancellation of this first order effect. The specific net change, therefore, is much smaller than the average change for an individual orbit.

A minimum requirement to accurately model resonant dynamics is that the resonant potential is well-populated by particle orbits. Since the change in any individual orbit as it passes through the resonance depends on the phase of the orbit, an accurate result relies on a dense sampling in phase. For a given resonant potential, there is a critical number of particles, f_{crit} , required to resolve the region near the resonance such that the response is represented by contributions from orbits at many phases. As explained in the previous paragraph, the change in the actions of any one orbit is first order in the bar amplitude, but these changes must cancel over the ensemble of orbits, leaving only the smaller second-order contributions that are responsible for long-term halo evolution. If phase space is incompletely sampled, the first-order changes will *not* cancel, but will produce random fluctuations and the real resonance-driven evolution will not occur.

Even when the resonance potential is well-resolved by particle orbits, it may still be rendered ineffective if potential fluctuations caused by the finite-number of particles swamp the resonant potential. It is possible to determine the power in the Poisson noise at any scale by Fourier analysis, or more generally from any orthonormal basis expansion that satisfies the Poisson equation in an axisymmetric coordinate system (Weinberg 1998). To resolve the resonance potential in the basis expansion, we require that the power in the coefficients of the halo response be greater than the power in the noise. Since a basis expansion is at the heart of our potential solver, we can use this signal-to-noise criterion to determine the critical number of particles needed to resolve the resonance potential for any expansion term used in our N-body simulation (see Paper II).

Noise on interparticle scales scatters orbits from their original trajectories and leads to a diffusion time scale that is unphysically short. If the diffusion time is shorter than the time that potentially resonant orbits would need to pass through a resonance driven by the slow evolution of the galaxy, the resonance will cease to exist. Without

these stable, resonant orbits, the exchange of angular momentum through this mechanism cannot take place. This diffusion on interparticle scales, i.e. *two-body relaxation*, is astronomically negligible for our bar–halo simulations, but can be a significant problem for other studies due to the numerical noise present in many N-body potential solvers. Since the phase-space width of the resonance is proportional to the strength of the bar perturbation, the time scale for drifting across the resonance can be a small fraction of the two-body relaxation time scale. However, direct summation, tree, and grid-based codes are all particularly prone to generating small-scale noise and are thus quite susceptible to rapid orbit diffusion. The only remedy is to increase the particle number while keeping the resolution fixed, thereby pushing the simulation toward the collisionless limit. Expansion codes still suffer from relaxation that will diffuse orbits in principle, but the *small-scale* noise is removed by truncating the expansion.

3. Numerical Techniques

3.1. N-body code

The disk and dark matter halo are evolved using a 3-dimensional self-consistent field (SCF) code (Weinberg 1999). In most N-body methods, it is either the gravitational softening introduced to decrease two-body scattering, or the grid cell size that determines the spatial resolution. In such codes, the number of spatial resolution elements within the simulation volume determines the effective number of degrees of freedom, typically a very large number. SCF codes (Earn & Sellwood 1995, Clutton-Brock 1972, 1973, Kalnajs 1976, Polachenko & Shukmann 1981, Friedman & Polyachenko 1984, Hernquist & Ostriker 1992, Hernquist, Sigurdsson, & Bryan 1995, Brown & Papaloizou 1998, Earn 1996, Allen, Palmer, & Papaloizou 1990, Saha 1993) limit the number of degrees of freedom to decrease the small-scale noise, making this class of code ideal for the simulation of the long term evolution caused by resonant dynamics.

Our potential solver exploits properties of the Sturm-Liouville equation to generate a numerical bi-orthogonal basis set whose lowest order basis function matches the equilibrium model (Weinberg 1999). Many important physical systems

in quantum and classical dynamics reduce to the Sturm-Liouville (SL) form,

$$\frac{d}{dx} \left[p(x) \frac{d\Phi(x)}{dx} \right] - q(x)\Phi(x) = \lambda\omega(x)\Phi(x), \quad (1)$$

where λ is a constant and $\omega(x)$ is a known function, called either the density or weighting function. If $\Phi(x)$ and $\omega(x)$ are positive in the interval $a < x < b$, then the SL equation is satisfied only for a discrete set of eigenvalues, λ_n , with corresponding eigenfunctions $\phi_n(x)$. The eigenfunctions form a complete basis set (Courant & Hilbert 1953) and can be chosen to be orthogonal with the following additional properties: 1) the eigenvalues λ_n are countably infinite and can be ordered: $\lambda_n < \lambda_{n+1}$; 2) there is a smallest non-negative eigenvalue, $\lambda_1 > 0$, but there is no greatest eigenvalue; and 3) the eigenfunctions, $\phi_n(x)$, possess nodes between a and b , and the number of nodes increases with increasing n , e.g. the eigenfunction $\phi_1(x)$ has no nodes, $\phi_2(x)$ has one node, etc.

In the special case of Poisson’s equation, we use the eigenfunctions to construct biorthogonal density and potential pairs, d_k and u_j , given by:

$$1/4\pi G \int dr r^2 d_k^*(r) u_j(r) = \delta_{jk}. \quad (2)$$

The lowest order potential-density pair ($n = 1$, $l = m = 0$) represents the equilibrium profile, and the higher order terms represent deviations about this profile.

For the equilibrium profile, we use a numerically relaxed and truncated form of the NFW profile as we describe below. We retain halo basis terms up to $n_{\max} = 10$ and $l_{\max} = 4$. For the disk, we derive a cylindrical basis from a spherical SL basis, using the empirical orthogonal function method described by Weinberg (1996, 1999). This method constructs a new linear combination of the original basis to closely match the disk profile. We derive the spherical disk SL basis from the deprojected disk profile using a large number of terms ($n_{\max} = 10$, $l_{\max} = 36$) to accurately resolve the thinness of the disk. Weinberg (1999) used a cylindrical solution of the SL equation to construct the empirical basis, a solution whose boundary conditions are inconsistent with the spherical halo basis; this motivated our use of a spherical SL basis for the disk as well. We retained ten basis functions

per azimuthal harmonic order, m , from this empirical basis set. The expansion parameters for each simulation (described below) are shown in Table 1. Particles are advanced using a leapfrog integrator, with a time step $h = 0.0002$, which is 0.008 of the smallest oscillatory period, the orbital frequency in the very central region, or $0.009 t_{\text{dyn}}$ at a disk scale length.

3.2. Generating initial conditions

Our galaxy models have two components: a dark matter halo and an initially bar-less, bulge-less exponential disk. The axisymmetric disk density profile is:

$$\rho_d(R, z) = \frac{M_d}{8\pi z_0 R_d^2} e^{-R/R_d} \text{sech}^2(z/z_0), \quad (3)$$

where M_d is the disk mass, R_d is the disk scale length, and z_0 is the scale height. We truncate the disk at $20R_d$ and at $10z_0$. Since the excluded mass is so small, we do not adjust the total mass to account for this truncation.

We adopt an axisymmetric velocity dispersion in the disk plane ($\sigma_r = \sigma_\phi$) and set the radial velocity dispersion so that the Toomre stability parameter, Q , is constant at all disk radii. Hence

$$\sigma_r^2(R) = Q \frac{3.36\Sigma(R)}{\kappa(R)}, \quad (4)$$

where $G=1$, $\Sigma(R)$ is the surface density, and to produce good equilibrium models, κ , the epicyclic frequency

$$\kappa^2(R) = R \frac{d\Omega^2}{dR} + 4\Omega^2, \quad (5)$$

where Ω is the circular frequency, is derived from the actual particle distribution. We determine the vertical velocity dispersion, σ_z , by solving Jeans' equations in cylindrical coordinates assuming a steady-state disk:

$$\sigma_z^2(R) = \frac{1}{\rho_d(R, z)} \int_z^\infty \rho_d(R, z) \frac{\partial \Phi_{\text{tot}}}{\partial z} dz, \quad (6)$$

where Φ_{tot} is the combined disk and halo potential. The mean radial and vertical velocities are zero, and the mean azimuthal velocity, \bar{V}_ϕ , is determined from the asymmetric drift equation:

$$\bar{V}_\phi^2(R) = V_{\text{circ}}^2(R) + \frac{R}{\rho(R)} \frac{d}{dR} [\rho(R) \sigma_r^2(R)], \quad (7)$$

where V_{circ} is the circular velocity derived from the combined halo-disk potential. We realize the velocities by approximating their distributions as Gaussians with the means and dispersions given above.

The dark matter halo density distribution is a truncated NFW profile. We use units where both the halo mass, M_{vir} , and the virial radius, R_{vir} , are one. Using these units, the density profile is:

$$\rho(r) = \frac{c^2 g(c)}{4\pi r(1+c)^2}, \quad (8)$$

where

$$g(c) = \frac{1}{\ln(1+c) - c/(1+c)}. \quad (9)$$

and c is the concentration parameter,

$$c = R_{\text{vir}}/r_s, \quad (10)$$

where r_s is the scale radius.

Since the NFW mass profile is logarithmically divergent at large radii, we truncate it at R_{vir} . However, an abrupt truncation of the density profile at the virial radius leads to a poor equilibrium, given our assumed isotropic velocity distribution. To generate a better equilibrium, we compute a phase-space distribution function with an isotropic velocity distribution by Eddington inversion (see Binney & Tremaine 1987) for the truncated halo and spherically averaged disk system combined. We generate a new halo density profile by integrating this phase-space distribution function over velocity. If an equilibrium model with an isotropic velocity distribution existed for the density profile, the new density profile would be identical. We repeat this procedure until the derived density profile does not change, which only takes a few iterations. The final halo density profile begins to noticeably deviate from a pure NFW profile at approximately $90\%R_{\text{vir}}$. We adjust the mass so that the total halo mass after this truncation procedure does not change. We realize the halo particle distribution and velocities simultaneously by Monte Carlo rejection using the phase-space distribution function.

Because we are investigating the long-term evolution of a galaxy, we take particular care to realize a stable equilibrium. Unfortunately, the stability of a cuspy profile is difficult to maintain with a finite number of particles, since the inner

TABLE 1
SIMULATION PARAMETERS

Run	Component	n_{\max}	l	m_{\max}	Mass	R_d	z_0	R_h	c
F,I,C,B	Disk ^a	10	0-36	4	0.06	0.01	0.001		
L	Disk ^a	10	0-36	4	0.06	0.01	0.001		
F,I,C,B	Halo	10	0,1,2,3,4	4	1			1	15
L	Halo	10	0,2,3,4	4	1			1	15

^aOnly the first $N_{\text{order}} = 12$ basis terms were included in the expansion. See Weinberg (1996) for details.

cusps will always be poorly resolved within some radius. This resulting lack of gravitational support causes the inner density profile to flatten within the poorly resolved region. To mitigate this problem, we generate our initial conditions in a three-step process. First, we populate the disk and halo phase space as described above. Then, we fix the disk potential and evolve the composite system for several dynamical times. This allows the inner halo to achieve a self-consistent equilibrium in the presence of the disk. The density profile turns over inside the empirically-determined ‘resolution limit’ of system, although it retains its NFW profile outside this radius. Typically, this resolution limit encloses about 20 particles out of our 5 million particle realization. Finally, we re-realize our initial conditions using this new self-consistent halo density profile. This process results in initial conditions that are remarkably stable in isolation; the Virial relation $2T/VC$, where VC is the Virial of Clausius, deviates from unity by less than 0.1% over 100 dynamical times at the disk scale length. For an 11 million particle simulation, the turn-over in the dark matter density profile occurs at approximately $1.5 \times 10^{-4} R_{\text{vir}}$, and occurs at $2.0 \times 10^{-4} R_{\text{vir}}$ and $2.5 \times 10^{-4} R_{\text{vir}}$ when using 5.5 and 1.1 million particles, respectively.

3.3. Bar formation

Bars can be triggered through global disk instabilities (Toomre 1964), or through secular growth (e.g. Polyachenko 1995). In N-body simulations of realistically hot disks, both mechanisms can

be overwhelmed by density perturbations that are caused by Poisson noise due to a finite-particle realization of the potential (Ostriker & Peebles 1973, Fall & Efstathiou 1980, Sellwood 1996). This may or may not reflect bar formation in nature, but does result in a large range in bar formation times. To control the onset time of bar formation, we trigger the bar by applying an external quadrupole potential. We adopt the quadrupole profile for a homogeneous ellipsoid with axis lengths $a : b : c = 0.02 : 0.01 : 0.001$ in model units. During the time the quadrupole is applied, it rotates at a fixed pattern speed with corotation at the semi-major axis of $a = 0.02$. The perturbation has the form $Y_{22}(\theta, \phi)\Phi_2(r)$, with

$$\Phi_2(r) \propto -A(t) \frac{r^2}{[1.0 + (r/b_5)^{5/\alpha}]^\alpha}. \quad (11)$$

The quantity b_5 describes the characteristic radius of the quadrupole; for $r \ll b_5$ ($r \gg b_5$), the quadrupole matches the inner (outer) solution of the Laplace equation. The exponent α determines the steepness of the central quadrupole potential; the sharpness of the turn over between the inner and outer Laplace solutions increases as α increases. The quadrupole fit to a homogeneous ellipsoid gives $\alpha \approx 5$. We adopt a time-varying amplitude of

$$A(t) = 0.25A_0 \left[1.0 + \operatorname{erf} \left(\frac{t - t_{\text{start}}}{t_{\text{grow}}} \right) \right] \times \left[1.0 - \operatorname{erf} \left(\frac{t - t_{\text{end}}}{t_{\text{grow}}} \right) \right].$$

(12)

We choose A_0 and a (which determines b_5) to match the quadrupole strength and length of a purely noise-driven bar in a 5.5 million particle simulation. We choose $\alpha = 1$, but the final bar profile is not sensitive to this value (see §5.2). For nearly all the externally triggered quadrupole runs, $A_0 = 0.4$, $a = 0.02$, $t_{\text{start}} = 0.05$, $t_{\text{end}} = 0.08$, and $t_{\text{grow}} = 0.03$. We choose the growth and damping time to be the dynamical time at the bar length, maximizing the orbit trapping efficiency of the external perturbation. This quadrupole perturbation is only non-negligible between at times 0.03 – 0.10 and, hence, the bar evolves self-consistently for $t \gtrsim 0.10$.

3.4. Experiments

We adopt a halo concentration of $c = 15$, consistent with CDM N-body simulations that take into account angular momentum transfer between the dark matter halo and baryons during galaxy formation (e.g. Jing 2000, Bullock et al 2001). We choose our units as follows: the halo mass is 1.0, the virial radius R_{vir} is 1.0, the disk scale length R_d is 0.01, the scale height z_0 is 0.001, and the total disk mass M_d is 0.067. In these units, the halo scale radius $r_s = 0.067$. These parameters are summarized in Table 1 and results in model galaxies with submaximal disks as shown in Figure 1 (left). To make it easier to compare with observed galaxies, we also scale the simulations to a typical dwarf galaxy and to the Milky Way. For the dwarf galaxy, we choose a circular velocity at the virial radius of 43 km/sec. For the Milky Way, we use the cosmological simulations of the local group by Moore et al (1998) as a guide, making the circular velocity at the virial radius 135 km/sec. All the resulting scalings are presented in Table 2. Throughout the text, whenever we quote a system unit, we will follow it by the equivalent dwarf and Milky Way scale in parentheses, i.e. (dwarf unit, Milky Way unit). For example, in the 5.5 million particle halo, the finite particle induced turn-over in the density profile occurs at 2.0×10^{-4} (12 pc, 60 pc).

We conducted 5 sets of simulations. The fiducial runs (Set F) include the external quadrupole trigger in a fully self-consistent halo and disk

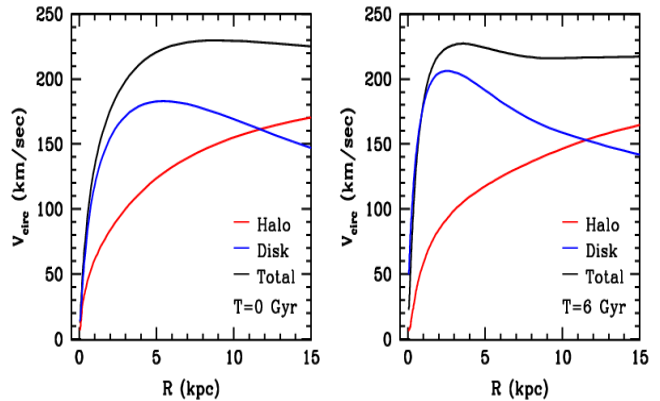


Fig. 1.— Initial and final rotation curves for our fiducial simulation. The model is scaled to Milky Way units to facilitate comparison to our galaxy. The black line is the total rotation curve, the red line represents the halo, and the blue line represents the disk. The inner halo expands while the disk contracts as discussed in §4.

model. We also run fixed-disk control simulations (Set C) for a consistency check on halo evolution. To ensure that the external quadrupole is not inducing the halo to evolve more than that of a bar formed through disk instabilities, we run fully self-consistent simulations that allow the bar to form on its own (Set I). Set L investigates a possible numerical artifact that could be introduced by the $l = 1$ portion of the potential expansion, and Set B tests the assertion (Sellwood 2002) that disks cannot form lasting bars much longer than the disk scale length. Each simulation is run for at least one time unit (1.3 Gyr, 2.2 Gyr) and as many as three time units (3.9 Gyr, 6.6 Gyr). Within each set, we vary only the particle number. The minimum number of halo particles used in any set is $N_{\text{halo}} = 10^6$, the maximum is $N_{\text{halo}} = 10^7$, and the disk particle number is always chosen to be $N_{\text{halo}}/10$. The subscript on the label for a particular run refers to the number of halo particles in units of one million. See Table 3 for a synopsis of the experiments.

4. The Fiducial Run

A bar clearly forms in our fiducial simulation (F_5). Figure 2 shows the face-on and edge-on view

TABLE 2
MODEL TO PHYSICAL UNIT CONVERSIONS

Galaxy Type	Length	Mass	Velocity	Time
Model	1.0	1.0	1.0	1.0
Dwarf	58 kpc	$2.5 \times 10^{10} M_{\odot}$	43 km/sec	1.3 Gyr
MilkyWay	300 kpc	$1.3 \times 10^{12} M_{\odot}$	135 km/sec	2.2 Gyr

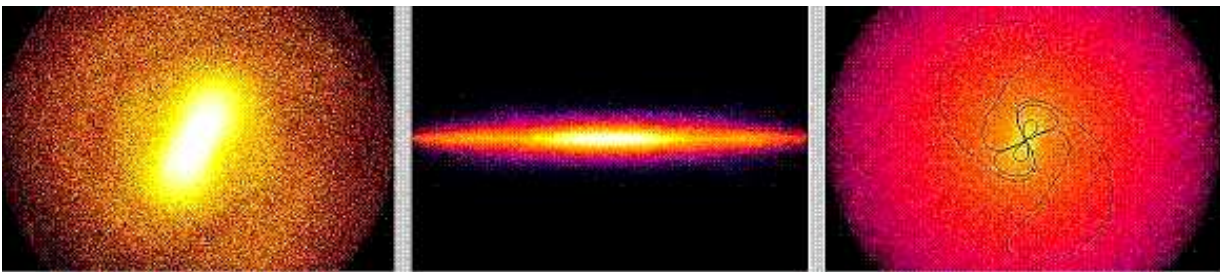


Fig. 2.— Surface density maps for the F_{10} run at $T = 0.18$ (234 Myr, 396 Myr). The brightness corresponds to the logarithm of the density with white being the most dense and black being the least dense over 5 orders of magnitude. The horizontal scale for each panel is $10 R_d$ (5.8 kpc, 30 kpc). The left panel is the face on view of the stellar component and the center panel shows the disk edge on. The right panel is the face on view of the dark matter particles, with a superimposed contour plot of the $m = 2$ component of the halo potential to accentuate the bar wake.

of the F_5 bar 0.18 time units (234 Myr, 396 Myr) after formation, as well as the wake induced in the dark matter halo by the bar.

The existence of a bar in such an initially cuspy system is a relatively new result; the large central mass of a cuspy halo can provide a barrier that prevents X_1 orbits from passing through the center (Binney & Tremaine 1987, Polyachenko & Polyachenko 1996). By removing such a major bar orbit family, this spherical potential barrier was thought to prevent the growth of a weak bar instability. Recent work by Athanassoula (2002) suggests that, contrary to hindering bar growth, cuspy dark matter halos encourage bar formation via resonant interactions that transfer angular momentum from the disk to the halo, consistent with our findings here.

In this section, we examine in detail the structural and kinematic evolution of the disk-halo system in our fiducial simulation. In addition, we explicitly demonstrate the importance of reso-

nant dynamics in this system through an analysis of halo orbits in resonance with the bar pattern speed.

4.1. Bulk characteristics

Determining the bulk properties of the bar is a notoriously ambiguous process. For example, several methods have been proposed to define bar length, ranging from the radius where there is an abrupt change in the measured ellipticity of the disk, to the radius where the amplitude of the $m = 2$ to $m = 0$ component of the disk drops below an empirically tested threshold. We choose to adopt as our bar parameters the length, mass, and ellipticity of a homogeneous ellipsoid fit to the $m = 2$ component of the disk potential (see eqn. 11), fixing the vertical height of the bar such that $c = b/10$. (See Figure 3 for a comparison of the projected best-fit ellipsoid and the projected bar surface density.) The bar has an initial length of 0.015 (0.87 kpc, 4.5 kpc), which is $1.5R_d$ for the

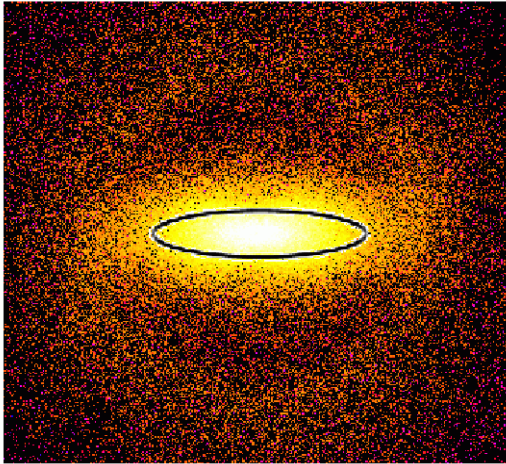


Fig. 3.— The bar length estimated from the best fit ellipsoid (black line) to the quadrupole part of the potential is over plotted on the surface density projection of the disk. Color scale is as described in Figure 2.

initial disk scale length of 0.01 (0.58 kpc, 3.0 kpc). The initial mass of the bar is $0.2M_d$ and the initial axis ratio is $b : a = 1 : 5$. The initial and final bar parameters for all the simulations are presented in Table 3

Figure 4 shows the time evolution of these quantities. Both the bar length and the mass grow by 60% over the course of the experiment, though the bar figure remains relatively stable. At first the axis ratio becomes somewhat rounder, going from $1/6$ to $1/4$ and then elongates once again to $1/6$. We also show the time evolution of the z-component of the moment of inertia, which nearly doubles. At later times, the moment of inertia of the bar increases as more particles from larger radii join the bar pattern, i.e. as the bar lengthens. The bar pattern also rapidly slows; over the course of the simulation, the bar slows to about 30% of its original rotation speed. A common way to express the rotational speed of the bar is by the quantity D_L/a_B , where D_L is the radius of corotation and a_B is a measure of the length of the bar’s semi-major axis. Initially, D_L/a_B is nearly 1, consistent with the pattern speeds in barred systems such as NGC 1365. However, by the end of the simulation, D_L/a_B rises to 2.2, far slower than any observed bars (Debatista & Williams 2000, Merrifield &

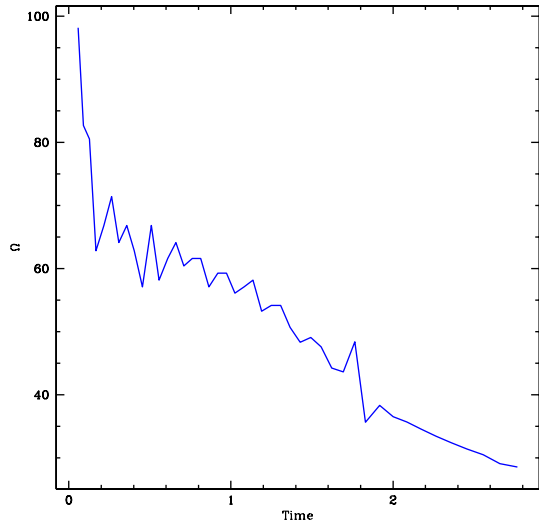


Fig. 5.— The pattern speed of the bar as a function of time for simulation F_5 .

Kuijken 1995, van Albada & Sanders 1982). Our strongly slowing bars are consistent with Debatista & Sellwood (2000) who found that bars slow significantly in a cuspy dark matter halo. If the moment of inertia were constant, the drastic slowing of the bar would imply that it lost 70% of its original angular momentum. The doubling of the moment of inertia lowers this angular momentum loss to about 40% of its initial value.

4.2. Angular momentum deposition and the slowing of the bar

The evolution of any collisionless system is governed by the transfer of angular momentum between global modes, or patterns, and individual orbits. In the case of a barred galaxy, angular momentum exchange between the bar and the halo or outer disk facilitates the bar’s formation (Athanasoula 2002), and causes the bar to slow its rotation (Tremaine & Weinberg 1984, Weinberg 1985, Debatista & Sellwood 2000, Athanassoula 2003). However, previous self-consistent simulations have disagreed on the role of angular momentum transfer, the relative importance of the disk-to-halo angular momentum exchange, and the magnitude of the resultant bar slowing.

Figure 6 plots the angular momentum evolution

TABLE 3
BAR PARAMETERS

Run	N_d	N_h	$l_{B,\text{init}}^{a,c}$	$M_{B,\text{init}}^{b,c}$	b/a_{init}^c	$l_{B,\text{final}}^d$	$M_{B,\text{final}}^b$	b/a_{final}	Time	Cusp Disrupted?
F ₁	1×10^5	1×10^6	0.018	0.018	1/4	0.024	0.03	1/5	2.38	no
F ₅	5×10^5	5×10^6	0.02	0.02	1/5	0.026	0.025	1/6	3.0	yes
F ₁₀	1×10^6	1×10^7	0.02	0.021	1/4	0.025	0.024	1/6	1.0	yes
I ₅	5×10^5	5×10^6	0.021	0.02	1/4	0.023	0.022	1/5	1.5	yes
L ₅	5×10^5	5×10^6	0.017	0.018	1/5	0.023	0.026	1/5	1.8	yes
B ₅	5×10^5	5×10^6	0.035	0.03	1/6	0.04	0.035	1/6	2.4	?

^aThe initial $R_d = 0.01$

^b $M_d = 0.067$

^cHere, the initial values are measured at $t = 0.2$

^dThe final $R_d = 0.004$

of the halo, disk, and bar, separately. Overall, the halo gains $0.0161J_{\text{init}}$ of the initial total angular momentum, J_{init} , and the disk loses $0.01648J_{\text{init}}$. The total angular momentum of the system is conserved to better than 0.4% over this time. As anticipated from the results of Papers I and II, the bar mediates this angular momentum transfer, both from the bar to the outer disk and from the disk to the halo. The bar loses $0.30J_{\text{init}}$ over the course of the simulation, with about half being transferred to the remaining disk and half to the dark halo. Figure 7 shows that most of the angular momentum loss within the disk occurs inside the radius of corotation, $0.28J_{\text{init}}$. However, this is less than the $0.30J_{\text{init}}$ lost by the bar, which approximately extends out to the corotation radius. Hence, the material not in the bar but within corotation gains about $0.02J_{\text{init}}$. This gain could be associated with the lengthening and strengthening of the bar. Also in Figure 7, one sees that between corotation and the Outer Lindblad Resonance (OLR) the disk loses $0.03J_{\text{init}}$ and beyond OLR gains $0.15J_{\text{init}}$. Of the $0.16J_{\text{init}}$ gain in angular momentum by the dark halo, roughly 19% is gained within corotation, 19% between corotation and OLR, and 62% beyond OLR. This qualitative behavior follows the expectations of linear theory. Strong resonances in the outer disk and halo

are responsible for most of the angular momentum exchange from the bar. In detail, however, things could be more complicated. Angular momentum could be exchanged between different parts of the halo and disk in addition to those processes implied by the simple angular momentum accounting above. For example, regions in the halo well beyond OLR actually lose angular momentum, implying that some additional angular momentum exchange must occur.

As described in §2, near a resonance, the fractional change in the angular momentum of an individual orbit is first order in the perturbation, and the sign of the first-order changes are anti-symmetric about the location of the resonance. The total angular momentum gains and losses at a given time for individual orbits are large, but the net change in the halo’s angular momentum is second order, and results from the near cancellation of this first order effect. Figure 8 shows both the large instantaneous gains and losses of angular momentum by individual halo orbits versus time and the much smaller gains in angular momentum made by the entire halo, confirming these theoretical ideas.

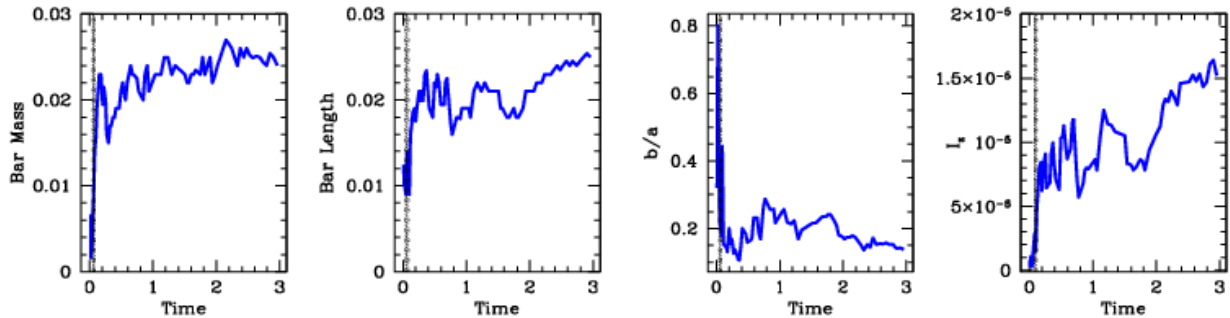


Fig. 4.— The bar mass (far left panel), bar length (left center), minor to major axis ratio (right center), and the z-component of the moment of inertia (far right) as a function of time for the fiducial run (F_5). The vertical line is the time when the triggering quadrupole stops.

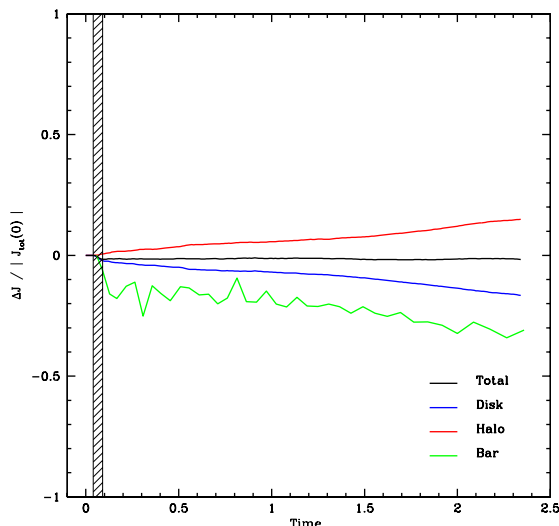


Fig. 6.— The fractional change of angular momentum in each component, normalized by the initial total angular momentum for simulation F_5 .

4.3. Resonances excited by interactions between the bar and halo

If an N-body system has the correct numerical characteristics to properly follow the important physical processes, linear perturbation theory predicts that angular momentum exchange will take place *only* at confined islands in phase space, the regions that correspond to halo-bar resonances (as

described in §2 and Paper II). The planar resonances for a bar rotating with frequency Ω_{bar} take the form:

$$l_r \Omega_r + l_\phi \Omega_\phi = m \Omega_{\text{bar}}, \quad (13)$$

where Ω_r and Ω_ϕ are the radial and azimuthal orbital frequencies, respectively, l_r and l_ϕ are integers, and m is the azimuthal multipole index. Ignoring phase, there are two non-degenerate actions, or conserved quantities, for a spherical halo, e.g. energy E and angular momentum J . The resonant condition therefore describes a curve in E - J space. Contours of angular momentum change in this space occur in positive and negative pairs, as orbits either gain or lose angular momentum depending on their direction of precession just before resonance in the bar’s rotating frame.

Figures 9–10 show the change in angular momentum of halo particles between two times, T_1 and T_2 . The halo phase-space distribution is plotted in the E, κ plane, where E is the total energy of the orbit, and $\kappa = J/J_{\text{circ}}$ is a measure of the orbit’s eccentricity ($\kappa = 0$ and 1 correspond to radial and circular orbits, respectively). Contours in these figures depict the change in the z-component of the angular momentum, ΔL_z . In addition, over plotted and labeled are the loci of resonances described by equation (13) directly derived from the N-body phase space at T_1 . These are typically near vertical lines for our equilibria.

In Figure 9, we plot the evolution between $T_1 = 0.5$ (0.65 Gyr, 1.1 Gyr) and $T_2 = 0.8$ (1.04 Gyr,

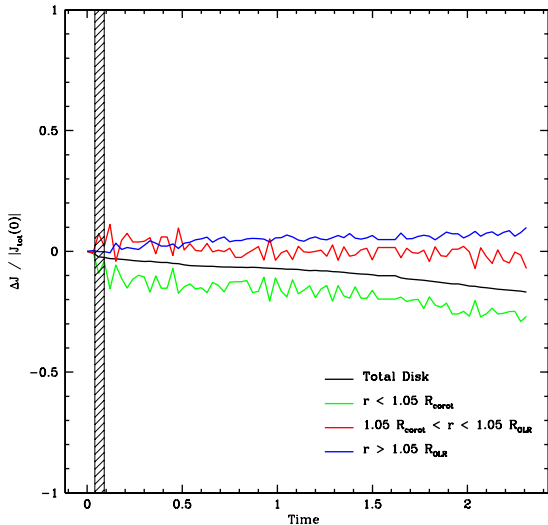


Fig. 7.— The fractional change in angular momentum of the disk for three different radial regions, normalized by the total initial angular momentum. The bar length is $R = 0.018$ at $T = 1.5$, and at this time, $R_{\text{corot}} = 0.026$, and $R_{\text{OLR}} = 0.045$.

1.75 Gyr), after the bar has completed approximately 10 rotations. At this point, the bar has a stable figure and pattern speed and the resonance signature is unambiguous, with nearly all the angular momentum exchange in the halo restricted to easily identifiable low-order resonances with the bar’s rotation. The main participants in this exchange are the corotation resonance ($0 : 2 : 2$), the Outer Lindblad Resonance ($1 : 2 : 2$), and resonances at $2 : 2 : 2$ and $3 : 2 : 2$.

Figure 9 shows the phase-space locations that dominate the angular momentum lost by the bar and are important for bar slowing. However, since halo orbits have differing amounts of angular momentum, the ΔL_z contours shown in Figure 9 are not useful for gauging the effects of angular momentum exchange on individual orbits or on the structure of the halo itself. In Figure 10, we plot the relative change in angular momentum over the same time period as in Figure 9. We quantified the relative angular momentum change by $\Delta J_z / J_{\text{tot}}$, where J_{tot} is the initial total angular momentum of an orbit. The largest relative change in angular momentum takes place within

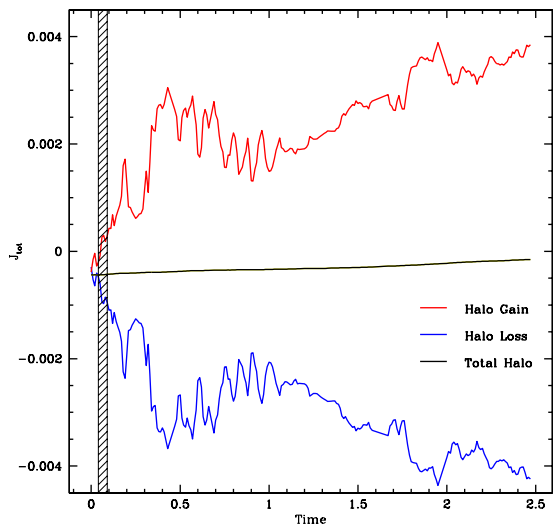


Fig. 8.— The sum of the angular momentum for halo orbits that gain (upper) or lose (lower) angular momentum together with the net gain (middle) as a function of time.

the central region, and the bulk of this change can be attributed to the Inner Lindblad Resonance ($l_r : l_\phi : m = -1 : 2 : 2$). The large relative gain in angular momentum by these central orbits causes the disruption of the halo cusp.

4.4. Density profile evolution

To interpret the effect of the bar on the halo, we must first assess the stability of the halo profile in the *absence* of a bar. Figure 11 shows the change in the density profile for the 5.5 million particle, fixed disk potential experiment (C_5). There is no appreciable change in the halo density profile over 3 time units (3.9 Gyr, 6.60 Gyr). When a bar is induced via an external quadrupole (F_5), the halo density profile changes dramatically, as shown in Figure 12. After $t = 1$ (1.3 Gyr, 2.2 Gyr), the halo profile begins to deviate from an NFW profile at $R = 1.67 \times 10^{-3}$ virial units (97 pc, 500 pc), quickly flattening to a $\gamma = 0$ cusp. At $R = 1 \times 10^{-3}$ (58 pc, 300 pc), the central halo density has decreased to half its original value. The bar-induced flattening continues to the end of the simulation at $t = 2.25$ (2.93 Gyr, 4.95 Gyr), producing a core of about $R = 3 \times 10^{-3}$ (170 pc, 900 pc).

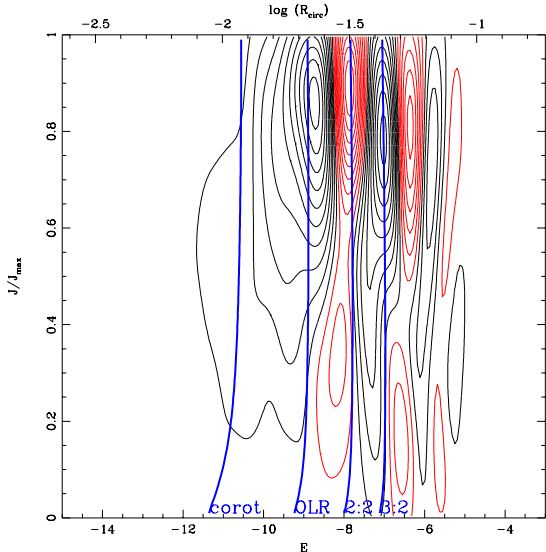


Fig. 9.— The angular momentum, ΔJ_z , exchanged between $T_1 = 0.5$ (0.65 Gyr, 1.1 Gyr) and $T_2 = 0.8$ (1.04 Gyr, 1.75 Gyr) for the entire phase-space distribution. The horizontal axis plots the total energy and the vertical axis plots $\kappa = J/J_{\max}(E)$, a measure of orbit eccentricity. The contours represent the difference in angular momentum between the two times for each point in phase space. Angular momentum gain (loss) is represented by red (black) contours. The nearly vertical lines are the positions of major resonances at time T_1 , and each are labeled.

Our experiments agree with the predictions of linear perturbation theory and with the idealized simulations of Paper II. These simulations investigate the halo evolution driven by the monopole and quadrupole terms of a rotating ellipsoidal bar with the same size, mass, and elongation as the the time average of the F series of experiments, in which the bar parameters remain fixed. The final density profile of this idealized simulation agrees with the fully self-consistent simulation (F_5), as plotted in Figure 12, which should be no surprise. Since the torque is applied to the halo orbits by the gravitational potential of the bar, as long as the quadrupole part of this potential in the N-body simulation is well-represented by the form of the quadrupole used in Paper II, the evolution and net angular momentum exchange will be similar. Although the core radii for the idealized simulation

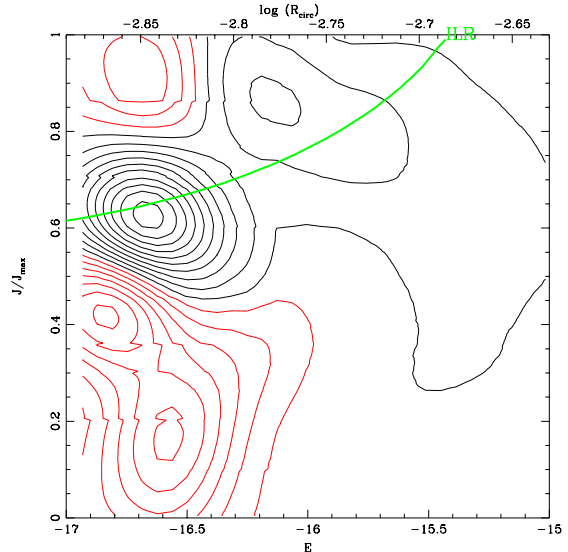


Fig. 10.— The relative angular momentum, $\Delta J_z/J_{\text{tot}}$, exchanged between $T_1 = 0.5$ (0.65 Gyr, 1.1 Gyr) and $T_2 = 0.8$ (1.04 Gyr, 1.75 Gyr) for the inner halo, as described in Figure 9. Only the inner region of the halo is plotted; outside this inner region, the relative angular momentum exchange is negligible.

and F_5 are similar, the central density of the idealized experiment is about 1.7 times smaller than in F_5 . The increased flattening occurs in the idealized run because the quadrupole is fixed over the entire experiment, while in the fully self-consistent simulation, the quadrupole strength is negligible until $T = 0.2$ (0.26 Gyr, 0.44 Gyr). The self-consistent bar structure changes only gradually after its initial formation, growing slightly more massive and more elongated as the galaxy evolves (see Fig. 4).

The final rotation curve for this simulation, plotted in Figure 1, shows that the disk density profile also evolves, becoming much more centrally concentrated as it responds to the loss of angular momentum. We plot the disk density profile explicitly in Figure 13. The inner disk becomes more dense as the scale length shrinks by 60% in response to angular momentum loss by the bar.

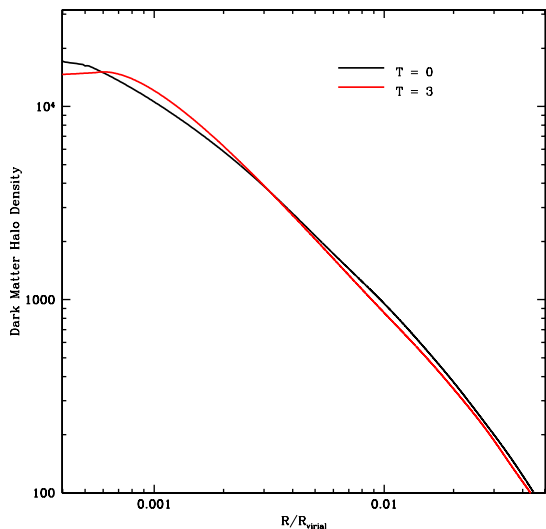


Fig. 11.— Initial and final halo density profiles for a halo with a fixed disk potential and 5 million particles (C_5).

5. Numerical Checks

Now that we have presented our basic results, it is necessary to determine their numerical robustness.

5.1. The effect of the $L = 1$ instability

If the disk were pinned to the initial origin of the simulation, as in the idealized simulations in Paper I, the evolution becomes sensitive to $l = 1$ instabilities. As the halo evolves, random fluctuations produce a small offset between the halo and the disk. This offset adds linear momentum to the halo, further increasing the offset, and leading to a rapidly saturating instability that artificially amplifies the halo cusp evolution. Paper I studied bar-induced halo evolution using an NFW halo and an external quadrupole designed to mimic a rigid rotating bar that was pinned to the origin throughout the simulation. This experiment had rapid halo evolution, although some fraction of it was a consequence of this centering artifact (Sellwood 2002, Paper II). Paper II shows that including a consistent response of the external quadrupole to the halo removes this artifact and the rapid halo evolution persists.

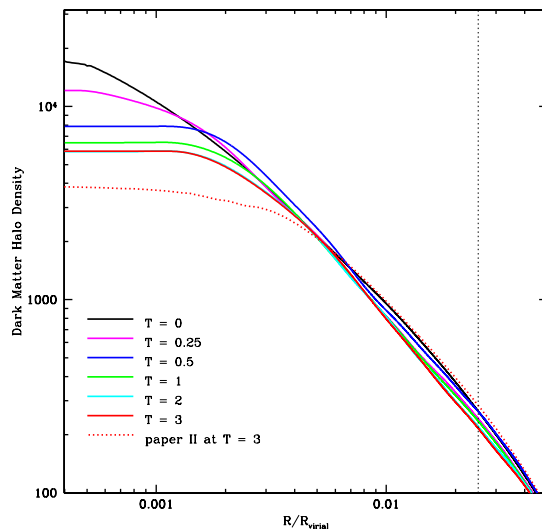


Fig. 12.— Initial and final halo density profiles for the fiducial experiment F_5 . See Table 2 for scaling to physical units. The bottom dashed line shows the final state for the idealized case from Paper II. The vertical dashed line shows the final bar radius.

The mutual response of the disk and halo in our fully self-consistent simulations should *automatically* act to damp this centering instability. Each component of the system responds to off-center density perturbations, which conserves total linear momentum. Hence, the fully self-consistent adjustment of the halo and disk centers prevents an $l = 1$ instability that artificially arises from a fixed center. To be certain that the evolution is not affected by this numerical artifact, we reran our fiducial simulations excluding the $l = 1$ term, i.e. including only $l = 0, 2, 3, 4$. If our evolution were effected by centering, these experiments would show less evolution than our fiducial runs. Figure 14 demonstrates that the halo evolution is similar to our fiducial F_5 experiment, giving us confidence that the halo evolution we see is unaffected by this centering-driven instability.

5.2. The effect of the external trigger

Figure 15 compares the projected density profiles of noise-triggered and external quadrupole-driven bars and shows that the initial bar length and strength are nearly independent of the trig-

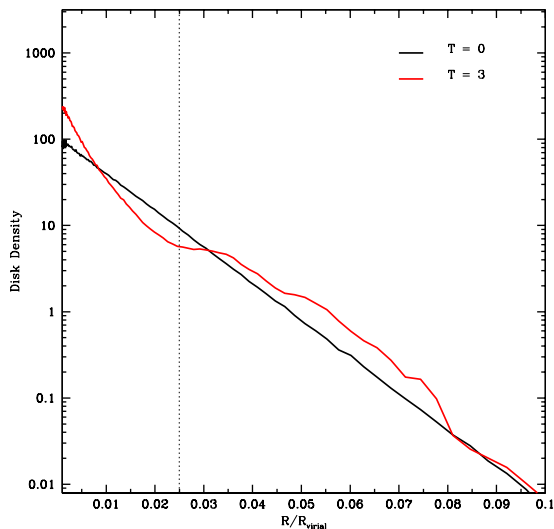


Fig. 13.— Initial and final disk density profiles for the fiducial experiment F_5 . The vertical dashed line shows the final bar radius.

gering mechanism. Unfortunately, neither bar has surface density profiles that are as flat as those observed in strongly barred galaxies (Kormendy 1982, Elmegreen & Elmegreen 1985); this is a common problem for bars produced in collisionless N-body simulations (Sparke & Sellwood 1987). However, a more realistic bar would have an even greater impact on the dark halo given its larger quadrupole. Figure 16 compares the potential in the $m = 2$ component of the disk at $t = 1$ (1.3 Gyr, 2.2 Gyr), long after the application of the external trigger, to the analytic potential provided by the quadrupole in equation (11) for integer values of α between 1 and 5. While the form of the potential used to trigger the bar initially is a centrally shallow $\alpha = 1$, the bar quickly evolves into one with a steeper potential. Hence, the bar evolution is independent of the precise form of the triggering potential. Furthermore, this comparison shows that the homogeneous ellipsoid is a reasonable choice to model the quadrupole potential of a self-consistent bar, as we do in Papers I and II.

When we allow the disk to form an approximately scale length-sized bar through noise-driven instabilities, the halo profile is flattened at nearly the same rate and to nearly the same radius as the quadrupole-induced bar (see Fig. 17). This simi-

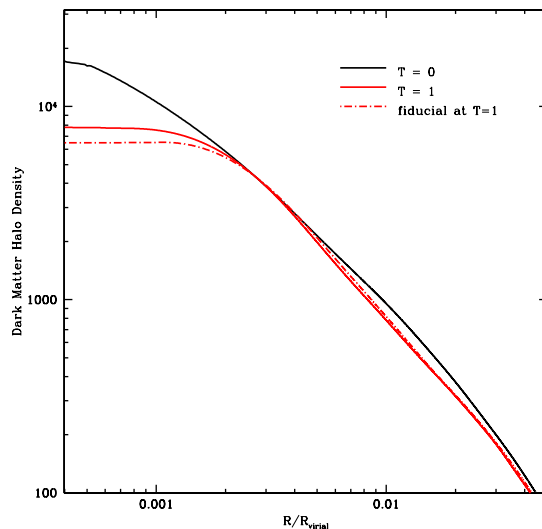


Fig. 14.— Initial and final halo density profiles excluding the $l = 1$ part of the potential expansion. The dashed line shows our fiducial (F_5) final state.

lar behavior from two very different bar-formation mechanisms shows that the response of the halo does not strongly depend on the bar triggering mechanism.

5.3. The effect of particle number

Even in state-of-the-art N-body simulations, the number of dark-matter particles is still *many* orders of magnitude smaller than those found in real galaxies. The errors introduced when the potential is realized in such a coarse manner can be significant. This leads to three possible sources of error: there may be an insufficient number of particles to allow the necessary first-order cancellation to take place near the resonance, the Poisson noise fluctuations from the discretely realized phase space can overwhelm the resonant potential, and the small-scale noise can scatter orbits so that they diffuse past the resonance, completely obliterating the resonant response. To properly resolve the slow evolution of a galaxy with an N-body experiment, it is critical to use enough particles to ensure that resonant orbits both exist in the model and are stable for astrophysically interesting time scales. Naturally, the minimum number of parti-

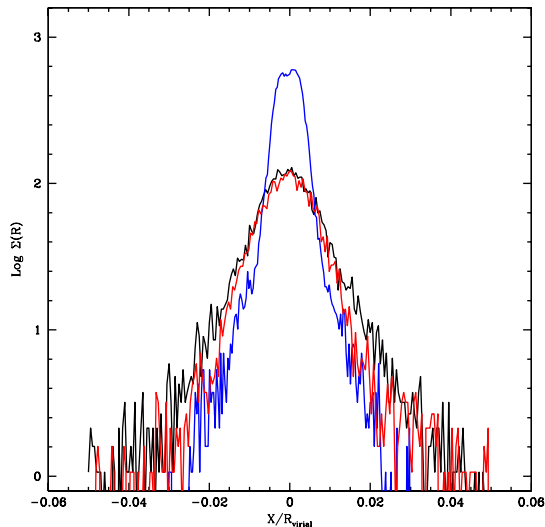


Fig. 15.— Surface density of the disk along the bar major axis for three different bar triggering mechanisms. The black line corresponds to a bar induced by an external quadrupole (F_5), and the red line corresponds to an instability triggered bar (I_5). The blue line represents the surface density of a bar formed in an adiabatically-grown disk, as will be discussed in §5.

cles needed to accurately track the dynamics depends on both the problem addressed and on the noise characteristics of the N-body code, so it is difficult to provide a universal particle number requirement. With current N-body technology, however, long-term evolution seems to require at least several million particles to fully resolve low order resonant interactions (Kandrup & Sideris 2002, Paper II).

Here, we empirically determine the critical particle number required to minimally resolve the resonant physics important for our problem, and elaborate on the problems faced when too few particles are used. In addition, we compare the particle number requirements derived here to theoretical criteria derived through perturbation theory analysis and using idealized N-body experiments in Paper II.

To ensure that the 5.5 million particle experiments are accurately resolving the dynamics, we compare both the evolution of 1.1 and 10 million

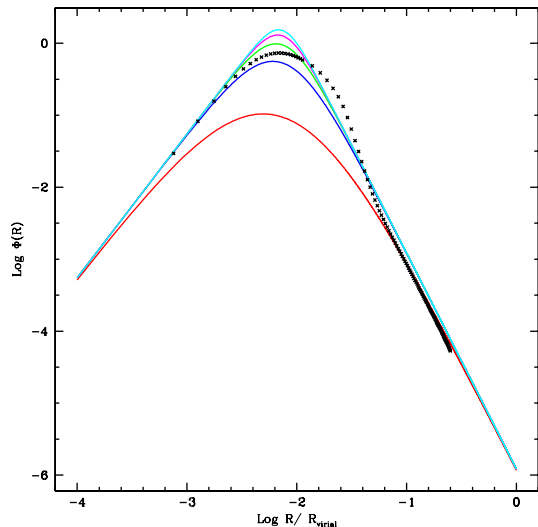


Fig. 16.— The quadrupole component of the gravitational potential of the bar. The black points represent the potential derived from the $m = 2$ component of the disk from our fiducial run (F_5) at $T = 0.9$ (1.2 Gyr, 2.0 Gyr). The solid lines correspond to integer values of $\alpha = 1, \dots, 5$ for the parameterized form of the triggering potential (eq. 11). The bottom curve corresponds to $\alpha = 1$ and the top curve to $\alpha = 5$.

particle simulations, F_1 and F_{10} respectively, to the fiducial 5.5 million particle run. Experiment F_{10} yields a nearly identical density evolution to that of our fiducial experiment, F_5 , implying that 5.5 million particles are sufficient for our numerical technique to resolve the dynamics of the bar-halo interactions responsible for driving cusp evolution. (Fig. 18). Therefore, we consider the halo evolution observed in our 5.5 million particle simulations to be a robust estimate of true resonant dynamics between a bar and halo. Conversely, the relative lack of density evolution in experiment F_1 , as evidenced Figure 19, implies that 1 million equal mass particles within the virial radius is not enough to properly resolve the dynamics. As we demonstrate below, the F_1 experiment appears to have been plagued both by insufficient particle number at the crucial resonances and by global potential fluctuations. These both act to severely underestimate the true density evolution of the halo.

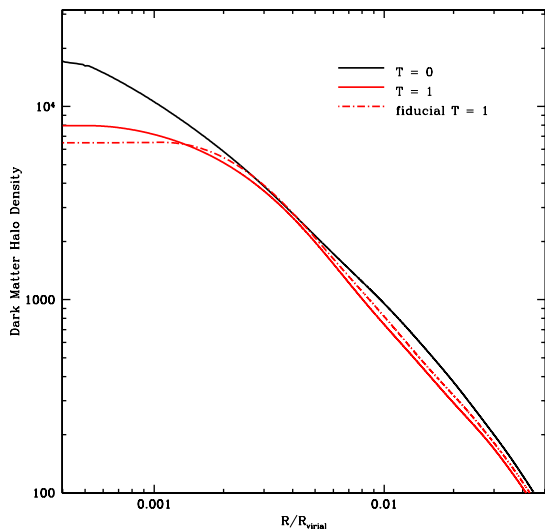


Fig. 17.— Initial and final halo density profiles for the experiment that allows the bar to form via internal instabilities (I_5). The density evolution is nearly identical to the triggered bar (F_5), plotted as a dashed curve.

As discussed in §2, any experiment designed to simulate resonant dynamics must have a well-populated resonance potential. This is the fundamental criterion, f_{crit} , derived in Paper II. For example, Runs F_5 and F_{10} show that the ILR is the most important resonance for increasing the angular momentum of the inner halo. The resonance potential for the ILR is global and extends from the center of the halo out to a significant fraction of the bar radius (see Fig. 3 of Paper II). At least a million particles are required to adequately sample the outer part of the resonant ILR potential, while approximately 10 million particles are needed to fully sample the innermost part of the resonance, which is crucial to the flattening of the halo cusp (Paper II). From this consideration alone, it is apparent that 1 million particle simulations will be unable to follow the halo evolution physics correctly. In fact, even our F_{10} experiments only minimally sample the entire ILR. It would be prudent to repeat all of these simulations with 10 times more particles to better sample the inner part of the ILR resonance, though this is beyond our current capabilities.

However, even when the resonance potential

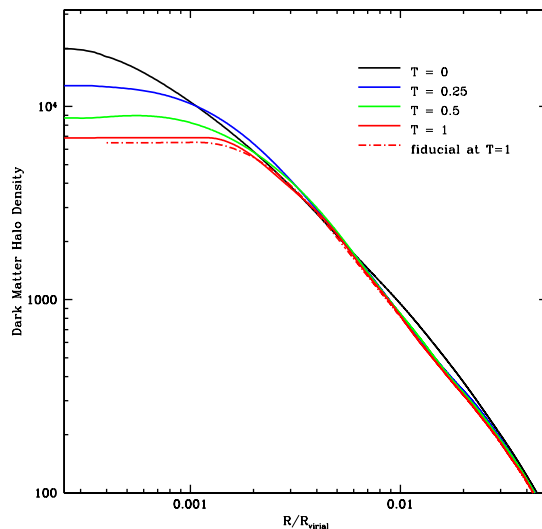


Fig. 18.— Initial and final halo density profiles of our fiducial triggered bar simulation using 10,000,000 particles (F_{10}). The dashed line shows the density profile in the 5 million particle simulation (F_5) at $T = 1.0$ (1.3 Gyr, 2.2 Gyr).

is well-sampled, Poisson noise from the finite-particle realization of the potential can overwhelm the resonant potential. An appeal to Poisson statistics demands that the F_1 run suffers from larger potential fluctuations. We can see the effect that these potential fluctuations have on the quadrupole component of the disk in Figure 20, which compares the power in the $l = m = 2$ harmonic for Runs F_1 and F_5 . The F_1 run features far less power in the $m = 2$ mode for both the disk and the dark matter halo (not plotted). Despite being triggered with the same bar strength, the F_1 bar fails to grow as strongly as in the F_5 simulation. We believe the excess non-physical noise in the 1 million particle simulation has damped the quadrupole wake in the halo.

Using the formalism developed in Paper II, we can compare the power in the noise to the power in potential from our basis expansion. We find that a simulation that resolves up to $n = 10$ radial terms requires approximately 3.5 million particles to prevent Poisson noise from overpowering the signal of the resonant response. This critical number is similar to the signal-to-noise threshold de-

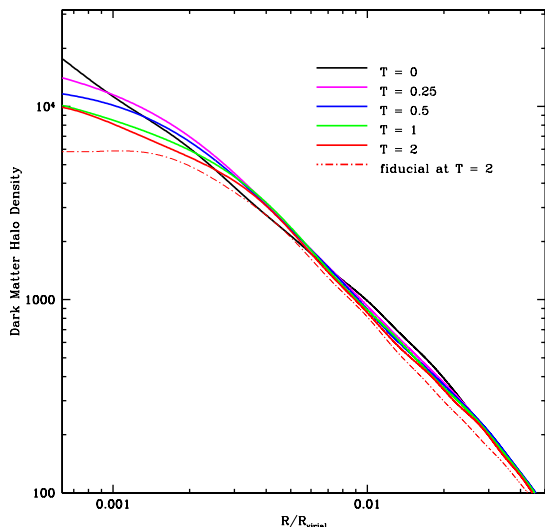


Fig. 19.— Initial and final halo density profiles for the triggered bar simulation using 1 million particles (F_1). The dashed line plots the F_5 density profile at $T = 2.05$ (2.7 Gyr, 4.5 Gyr).

rived in Paper II for 10 radial basis terms. Our use of orthogonal functions to estimate the power at particular scales is no different than any Fourier-based power spectrum: the maximum number of radial terms corresponds to smallest spatial scale. Other potential solvers, such as direct summation or tree algorithms, typically resolve many more length scales and consequently have many more degrees of freedom. Our estimate based on $n = 10$ radial basis terms will place a lower limit on the particle requirement for these other methods.

Using these criteria, the reason for the lack of evolution in the F_1 experiment is clear: it is impossible for 1 million particles to simulate the resonant dynamics.

6. Discussion

6.1. Resonances, particle number and comparison with other simulations

The agreement between the simulation results presented here and the predictions of both linear perturbation theory (Lynden-Bell & Kalnajs 1972, Tremaine & Weinberg 1984) and idealized halo-rigid bar N body simulations (Papers I & II)

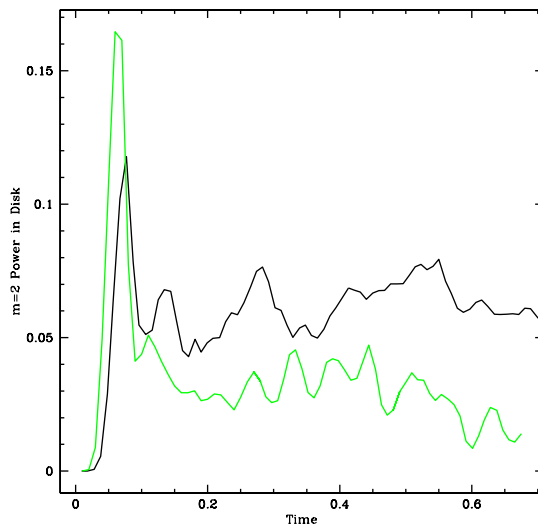


Fig. 20.— The relative power in the $m = 2$ component of the disk potential for the F_5 (black) and F_1 (green) simulations. After the external trigger is complete at $t = 0.1$, the better resolved run obtains much more $m = 2$ power, while the $m = 2$ power in the poorly resolved experiment remains relatively constant.

provides us with a firm physical foundation to interpret our results. We have demonstrated microscopically that resonances mediate the angular momentum transfer and drive the structural evolution, a point recently emphasized by Athanassoula (2003) in studies pertaining to bar growth. Differences with other recent studies may be explained either by differences in the bar shape or by noise effects owing to insufficient particle number as described in §2 and §5.3, or both.

In these recent studies, the halo is represented as an approximation of a smooth system, yet approximately 10% of the mass within a dark matter halo is contained within clumps between 10^8 and $10^{10}M_\odot$ (Moore et al. 1999b, Font et al. 2001). This substructure noise spectrum provides large, low frequency fluctuations and Weinberg (2001ab) shows that resonance driven evolution does occur in the presence of this real astronomical noise. In contrast, N -body discreteness noise generates high spatial frequency fluctuations that drive evolution by local diffusion. A sufficiently

rapid drift in orbital frequencies decouples orbits from any resonances and diminishes or eliminates the torque. Therefore, noise on interparticle scales has very different consequences than large-scale dark matter substructure. Although astrophysical noise is most certainly an important contribution to galaxy evolution, astrophysical and numerical noise sources have different effects on the evolution studied here. Astrophysical noise causes the location of resonances to slowly change while numerical noise causes them to disappear.

We have presented two particle number criteria necessary for resonances to be effective (see Paper II for details) and have tested them empirically. For equal mass halo particles, at least 5 million particles are required within the virial radius to fully resolve the resonant physics. A third criterion requires a sufficient particle number so that an orbit does not diffuse away from resonances; we defer development of this to a later paper. This orbit diffusion criterion is not critical for our SCF N-body method, but might prove to be the most restrictive for direct summation, tree or grid based techniques.

Spatially adaptive codes such as direct summation, multigrid or tree codes can resolve acceleration from structures on many scales. This is a great advantage when simulating large-scale structure, but unfortunately also allows noise to appear at all scales. At small scales, this noise is dominated by finite particle sampling rather than astronomical structure. In contrast, our SCF expansion method selectively filters the small Poisson-dominated scales, reducing the small scale noise by at least an order of magnitude. Even though the small scale noise is reduced, our choice of expansion parameters still allows us to fully resolve the resonances themselves. Any further increase in spatial resolution runs the risk of adding to the numerical noise and removing the resonances.

Even though the resonances responsible for slowing the bar occur at large radii and are, therefore, easier to accurately resolve, we suspect that the noise characteristics of many widely-used potential solvers have suppressed the torque in those studies that find little evidence for bar slowing. The numerical criteria for accurately evolving the cusp are more stringent, both because the resonances responsible for the cusp evolution extend to much smaller radii where there are fewer particles

and because the resonance responsible has a much weaker, more shallow potential. We suspect that many studies that fail to find cusp evolution are not adequately resolving the central resonances.

We show in Paper II that the bar slow down rate and the change in the halo density profile depend sensitively on the shape, amplitude, and size of the bar. Bars with a smaller amplitude take longer to slow, have less effect on the cusp, and are more numerically difficult to evolve correctly due to the shallower resonance potential. Although the size of the bar does not greatly effect the slow down rate, a highly centrally concentrated bar has a larger fraction of the power in the $m=0$ mode, and with less $m=2$ power it is less capable of driving cusp evolution. Smaller bars are also more numerically difficult to evolve accurately since the resonances lie at smaller radii. These numerical and physical effects combine to make simulating the evolution of galaxies with small, weak bars particularly subtle.

For example, VK perform simulations of bars using the Adaptive Refinement Tree (ART) potential solver (Kratzov, Klypin & Khokhlov 1997), allowing the bar to form through local instabilities and following its evolution. They find that a bar forms with a radius about equal to that where the rotation curve stops rising, that the bar does not slow appreciably, and that the central dark matter cusp is not removed. All of their differences with our results can be easily explained by their inability to properly follow the resonant dynamics. It prevents their bar from secularly growing and it remains small. Since resonances mediate the angular momentum exchange between the halo and the bar, the bar will not slow and the cusp will not evolve if the resonances are removed. Their simulation with the largest particle number, $N = 3.55 \times 10^6$ particles within the virial radius, satisfies our necessary criteria for populating the resonances in phase space. This number of particles is also enough to suppress fluctuations on the scale of the resonant potential, though more particles are required due to their higher spatial resolution. Their multimass technique partly but not entirely mitigates the problem by concentrating more particles in the central region, making their particle number equivalent to 9.5×10^6 .

However, this and any mesh-based N-body technique suffers from numerical artifacts that ar-

tificially decrease the 2-body relaxation time scale (Gneidin & Bertschinger 1996, Dehnen 2001). The short diffusion time scale may scatter orbits too rapidly for resonant angular momentum coupling to take place. Although we cannot determine the diffusion time scale in the VK experiments without their initial conditions and code, previous comparisons of the noise characteristics of tree and expansion codes indicate that about 2-4 times more particles are required for a tree code to achieve the same diffusion time scale as an equally-smoothed SCF code (Hernquist & Ostriker 1992, Barnes 1997), implying that a 20 million particle simulation would be required to achieve stable orbits in the halo for a standard grid based code with our spatial resolution. VK also have extremely high spatial resolution, which further exacerbates the small scale noise problem and would require even more particles, as discussed in the previous paragraph.

Furthermore, the orbit diffusion problem is even more acute in the ART code. Adaptive refinement serves to better resolve regions of high density, making this an excellent technique to model the halo cusp. However, if the mesh used to determine the potential is not adjusted often enough to respond to the changing system, as in the simulations of VK, the particles can experience unnaturally large accelerations across mesh boundaries that are unrelated to the true potential (Jesop et al 1994, Anninos, Norman, & Clarke 1994, Kravtsov, Klypin, & Khokhlov 1997). VK choose to regrid only after many particles enter a grid cell to reduce run time. Particles within a grid cell are free to drift relative to one another until regridding occurs. If particles have drifted close together, when regridding occurs, they will suffer artificially large Fermi accelerations that will scatter the orbits and pump energy into the system. This will greatly increase the orbit diffusion and swamp the resonant bar-halo interactions. Hence, the lack of inner halo evolution and the comparatively smaller overall bar-halo torque reported by VK might be partly caused by their technique.

Sellwood (2002) also studied the formation and evolution of bars that formed through local instabilities using a grid based approach. He forms a bar that is both weaker and more centrally concentrated than those in our simulations (e.g. I_5). It slows, but does not affect the central dark matter

cusp. His largest simulations contain 21 million particles, enough to satisfy both of our criteria for properly evolving resonant dynamics but perhaps not enough to sufficiently reduce orbit diffusion. He also uses different initial conditions than either us or VK. He uses a Hernquist profile instead of an NFW profile and, more importantly, instead of starting with an equilibrium model he grows the disk adiabatically.

To investigate the effect of Sellwood's disk growth procedure, we adiabatically grew an I_5 disk in an initially I_5 halo (see Table 3), allowing the bar to form by instability. The surface density profile of the resulting bar is sharply centrally peaked, shown in Figure 15, as it also appears to be in Figure 6 of Sellwood (2002). The self-consistent bar in the Sellwood study is unlike both the fiducial bar in our work and observations of most strong bars, which have constant surface density profiles (Kormendy 1982, Elmegreen et al. 1996). Such a highly centrally concentrated bar is less capable of driving cusp evolution. In addition, the bar appears to be much weaker than in I_5 . Our adiabatically formed disk is 1.5 times hotter than the one in our equilibrium initial conditions, and Sellwood's use of a rather low disk to dark halo mass ratio of 0.05 further raises the Q value; local instability triggered bars in hot disks are smaller and weaker. Since halo evolution scales with the bar mass, we believe the lack of halo evolution is likely a consequence of an anomalously weak quadrupole. Finally, since it is more numerically challenging to evolve smaller, weaker bars, Sellwood's simulation might not be able to resolve the inner resonances responsible for the cusp evolution but still be able to resolve those responsible for slowing the bar.

Athanassoula (2003) presents self-consistent N-body simulations of a forming and evolving bar using a direct summation approach implemented with GRAPE. Her bars form through local instabilities and many of her results are consistent with our findings. Most of her bars slow and she shows that angular momentum transfer to the halo, mediated by resonances, determines the slow down rate. Although not discussed in the text, her Figures 8 and 12 clearly indicate a reduction in the central dark matter density. Her halo profile is an isothermal sphere with a core truncated at about 1/9 the virial radius. In her typical experiment,

she uses 2 million particles, which would be equivalent to about 10 million particles if she simulated an NFW profile that extended to the virial radius. In addition, she uses a multimass technique that further increases her effective particle number to at least 25 million. Once again, this is enough particles to satisfy both of our particle number criteria for properly evolving the resonant dynamics but perhaps not enough to sufficiently reduce orbit diffusion in a direct summation code.

However, in her run that best matches our fiducial simulation, MHH2, the change in the bar pattern speed was about 3.5 times smaller than ours. This run features a more extended halo, based on set of initial conditions that add a second component with larger extent and a larger core. She finds that bar slow down rate decreases with increasing halo extent and attributes this trend to a higher velocity dispersion in the more extended halos. Although this could in theory explain her results, Athanassoula’s experiment does not represent a fixed profile successively truncated at smaller radii. She increases the extent of her initial halo by adding a component with a larger core radius. This new profile increases $M(< r)$ not only in the outer parts but at all radii, which not only changes the velocity dispersion, but also changes the dark-matter gravitational potential and, hence, the orbital frequency distribution near the bar. In Paper II we perform simulations using our idealized bar model with NFW profiles truncated from $0.3R_{\text{vir}}$ to $2.0R_{\text{vir}}$. In all cases, the bars slow down at roughly the same rate and the velocity dispersions at the bar radius do not measurably change. The velocity dispersion only changes significantly near the truncation radius.

Moreover, Athanassoula’s extended halos modify the stability of the disk, i.e. the dispersion relation, by contributing additional gravitational support, thereby modifying the length and shape of the forming bar. In fact, the bars that formed in her multicomponent halo systems are smaller and weaker than those in the single component halos (Athanassoula 2003, her Fig. 8). The shape of the bar’s quadrupole critically determines the strength of the coupling with the halo as a function of radius (see Paper II). This both explains the differing torque estimates and suggests that the trends reported in Athanassoula (2003) may depend sensitively on both the bar shape and halo

profile. In addition, smaller bars require a larger number of particles to adequately resolve the resonances and too few particles could systematically diminish the torque.

Bars form through the secular growth of features either triggered by local instabilities or externally, e.g. by satellite encounters. Resonant angular momentum exchange with both the dark halo and the outer disk facilitates this secular growth (Athanassoula 2003). Hence, to accurately simulate bar growth one must properly simulate resonant dynamical processes, requiring the simulation to meet all the numerical criteria discussed above. The size and strength of bars that form through local instabilities depend on the stability of the disk, i.e. disks with lower Toomre Q values will form stronger bars than those with larger Q values. Since the formation of a local instability triggered bar depends on the existence of an ILR, the initial bar sizes are restricted to the rising part of the rotation curve. However, secular growth can further increase the bar size well into the flat part of the rotation curve. In the simulations of Athanassoula (2003), bars form through local instabilities that are two to four times larger than the radius where the rotation curve becomes flat. In contrast, when bars form due to an external trigger, even their initial size is not restricted to the rising part of the rotation curve. The large imposed quadrupole potential from the tidal trigger overwhelms the “donkey star” growth criterion (Lynden-Bell & Kalnajs 1972) based on the underlying potential alone. Similarly, a tidal trigger nullifies formation arguments based on swing amplified instabilities (e.g. Mayer & Wadsley 2003). To demonstrate this, we perform a simulation (B_5) where we externally trigger and form a large stable bar using our fiducial simulation (F_5) parameters, but with a quadrupole scale length that is twice as large. The bar forms with a radius of $R = 0.04$ (2.3 kpc, 12 kpc) after $t = 1.5$ (2.0 Gyr, 3.3 Gyr), as shown in Figure 21. Remember that the disk had an initial scale length of $R = 0.01$ (580 pc, 3 kpc) and that the rotation became flat at $R \sim 0.01$ (580 pc, 3 kpc).

6.2. Comparison with observations and Λ CDM galaxy formation scenarios

Our N-body experiments demonstrate that an initially corotating, scale-length sized bar will gen-



Fig. 21.— Face on view of a $R = 0.04$ (2.3 kpc, 12 kpc) externally triggered bar (B_5) after $t = 1.5$ (2 Gyr, 3.3 Gyr) in a disk with an initial scale length of $R = 0.01$ (580 pc, 3 kpc).

erate a core in the density profile that extends out as far as $R = 0.003$ (170 pc, 900 pc). Current rotation curve decompositions of high surface brightness spirals (Salucci & Burkert 2000) suggest halo core radii of at least $R = 0.04$ (2.3 kpc, 12 kpc). The dynamics of the gas and stellar components may overwhelm the dark matter signal in these systems, however. Low surface brightness galaxies (LSBs) are thought to be dark matter dominated and can, therefore, be used to obtain a cleaner dark matter signal from the rotation curve. Typical halo core radii for low-surface-brightness galaxies range from 0.001 (60 pc, 300 pc) to 0.02 (1.2 kpc, 6 kpc). Hence scale-length-sized bars, like those studied here, cannot produce cores this large in cuspy Λ CDM density profiles.

However, the lengths of *tidally-triggered* bars can be over 10 times larger than those in our fiducial simulations. As we have discussed in the previous section, we form a bar four times our fiducial length through an external trigger (Fig. 21). Since linear perturbation theory suggests that the destruction of the halo cusp scales with the size of the perturbing quadrupole (Paper I, Paper II), we expect that larger primordial bars will generate proportionately larger cores.

A second possible solution invokes multiple

epochs of bar formation and destruction during the hierarchical assembly of the galaxy, which is characterized by relatively quiescent periods punctuated by mergers. Since conservation of phase space density suggests that the merger of two halos with a core also forms a halo with a core, the cores will persist as long as one or more bar phases occur sometime during the hierarchical assembly process. It is plausible that a new disk equilibrium is established after each merger event and that the quadrupole of the merger remnant will externally trigger a large bar. Minor mergers will also trigger bars without disrupting the disk. A larger core at the end of each merger-punctuated epoch facilitates the formation of a larger bar and subsequently a larger core. Taken more generally, our bar–halo mechanism predicts an intrinsic dispersion in galaxy properties owing to differences in evolutionary history: the present-day morphology will depend on whether or not a large bar was triggered, whether or not a standard bar is excited by astrophysical noise sources, and the overall merger history. This dependence can lead to galaxies with varying degrees of cusp flattening and disk scale-length evolution.

Since most of the evidence against central dark matter cusps in galaxies concerns low surface brightness dwarfs, one might not expect strong bars to form in such systems and, hence, for the mechanism proposed here not to have much relevance. However, the same analysis used to indicate the lack of a central dark matter cusp also shows that these low surface brightness galaxies are three or four times more baryon deficient than normal galaxies (Van den Bosch & Swaters 2001). If a strong bar forms in a gas rich disk of a dwarf galaxy, much of the gas will lose substantial amounts of angular momentum, be driven towards the center, undergo a strong starburst and, due to the shallow potential well of the dwarf galaxy, much of the gas could be expelled as a supernova-driven wind (Dekel & Silk 1986). The work done on the galaxy during this process will cause further expansion of the core. The remaining galaxy would be one of low surface brightness, possessing a core in its dark matter distribution. Our bar mechanism, therefore, not only provides a natural explanation for the existence of dark matter cores, but for the existence of low surface brightness dwarfs as well; those dwarf galaxies that had the

strongest bars will have the largest cores and the lowest surface brightness. Furthermore, Holley-Bockelmann, Katz, & Weinberg (2003) show that even low surface galaxies can form bars and remove their dark matter cusps.

Regardless of the scenario, we have set a lower limit to the size of the core generated by early bar-halo interactions. This lower limit already has implications that are astrophysically relevant. For example, Gondolo & Silk (1999) have argued that the cusps of dark matter halos may produce a neutrino signal from particle dark matter annihilation, though this requires that the cusp continues inward to 1 pc. Our experiments show that these neutrino signatures will not exist for any galaxy that has gone through a barred phase, unless a supermassive black hole has subsequently induced a cusp (Ullio et al 2002). In addition, spiral structure can also couple to the dark-matter halo with the same mechanism. Although spiral arms are weaker than bars, it is likely that modest spiral structure in the inner disk would be capable of affecting cusps at the parsec scale.

Bars are ubiquitously produced in galaxy simulations either through local instabilities or tidal interactions (Barnes & Hernquist 1992, Noguchi 1996, Steinmetz & Navarro 2002). Recent cosmological simulations designed to track the morphological evolution of galaxies predict that the bar phase is a natural byproduct of galaxy evolution (Steinmetz & Navarro 2002). An L_* Sb galaxy at $z = 0$ should have experienced a large bar by $z = 1.5$, and this should be observable with NGST. Both the higher galaxy gas fraction (Somerville, Primack, & Faber 2001) and the higher interaction rate (Le Fèvre et al 2000, Kolatt et. al. 2000) should enhance high redshift bar formation. Despite all this theoretical prejudice, the high redshift bar fraction of SB galaxies is claimed to be smaller than the local bar fraction: 5% for $0.6 < z < 0.8$ versus 30% in the local Universe (van den Bergh et al. 2002, Abraham et al. 1999). This might be a selection effect. For example, the identification of high redshift bars might be hampered by low sensitivity (van den Bergh et al. 2002). Moreover, the classification technique used to identify high redshift bars may misclassify bars undergoing strong starbursts (Jogee et al. 2002), a characteristic event for a newly-formed bar in a gas rich environment (Friedli & Benz 1993, Sheth

et al. 2002). In fact, recent NICMOS data have revealed that there is no significant evidence for a decrease in the fraction of barred spirals out to $z \sim 0.7$ (Sheth et al 2003). Answers to this mystery will help define the epoch of bar formation, constrain the “duty cycle” of bars and specify the role of bars in driving galaxy evolution through the mechanisms proposed in this paper.

7. Summary

Based on linear perturbation theory and idealized N-body simulations for the evolution of a rotating bar in a cuspy dark-matter halo, Weinberg & Katz (2002) predicted that the bar slows as it loses angular momentum to the halo and that the dark matter cusp flattens as it gains angular momentum. Resonant interactions between halo orbits and the orbiting bar perturbation causes this angular momentum transfer. We have performed high-resolution, self-consistent N-body simulations of realistic stellar disks embedded in NFW dark matter halos and have verified each of these predictions. Our overall specific conclusions are as follows:

1. The bar mediates significant angular momentum transfer in the galaxy, driving evolution in the disk and halo. Approximately 30% of the initial bar angular momentum is lost to the halo and outer disk after $t = 2.7$ (3.5 Gyr, 6 Gyr). The inner halo cusp is flattened to $R = 0.003$ (170 pc for a dwarf, 900 pc for the Milky Way) and the inner disk scale length shrinks by 60% for our $R = 0.05$ (870 pc, 4.5 kpc) bar. During this time, the disk transfers 16% of its initial total angular momentum to the halo through resonant interactions.
2. We empirically demonstrate the need for at least 5 million equal mass particles within the virial radius to correctly represent resonant dynamics using an expansion (SCF) N-body technique. There are two reasons for this. First, with too few particles, Poisson fluctuations in the gravitational potential can overwhelm the resonance potential. This is particularly important for the innermost ILR-like resonance that drives the cusp evolution. As the particle number decreases,

the resolved portion of this resonant potential lies further out in the halo, and the cusp evolution is suppressed. Second, the resonant torque is an ensemble effect, and therefore requires many particles near the resonance in phase space. Paper II presents explicit numerical criteria for both conditions that agree with our empirical findings. These particle number criteria are likely to be lower limits for potential solvers such as direct-summation, grid, or tree codes. These criteria also ignore the effects of orbit diffusion, which would further increase the required particle number for these methods.

3. A similarly shaped bar forms after stimulation by an external trigger or through an internal instability. The gravitational potential of either bar is well-represented by that of a homogeneous ellipsoid. The shape and amplitude of the bar's quadrupole determines the radial scale over which resonant coupling can occur. A bar with a more gradual profile, such as that used by Hernquist & Weinberg (1992) and by Sellwood (2003), provides a quadrupole thirty times smaller than that found here and than that used in Weinberg & Katz (2002), explaining the negligible evolution and slow down reported by Sellwood (see Paper II for details).
4. We agree with some aspects of previous simulations of bar formation and evolution. We attribute the differences to either the use of unrealistic initial conditions or to small-scale numerical noise that artificially removes the dynamically important resonances.
5. We have shown that a tidal interaction can induce strong bars to form, grow, and persist at many disk scale lengths, well beyond the rising part of the galaxy's rotation curve. Hence, the formation of large bars are compatible with flat rotation curve galaxies.
6. Bars, and other more general excitations, may reshape the halo structure for both high- and low-surface brightness galaxies and may affect a galaxy's morphological history. This complicates the interpretation of present-day rotation curves as probes of the primordial dark matter halo distribution.

KHB would like to thank Chris Mihos and Steinn Sigurdsson for helpful comments on an earlier version of this draft. This work was supported in part by NSF AST-0205969 and AST-9988146, and by NASA ATP NAG5-12038 and LTSA NAG5-13102.

REFERENCES

- Abraham, R. G., Merrifield, M. R., Ellis, R. S., Tanvir, N. R., Brinchmann, J. 1999, MNRAS, 308, 569
- Allen, A. J., Palmer, P. L., & Papaloizou, J. 1990, MNRAS, 243, 576
- Anninos, P., Norman, M. L., & Clarke, D. A. 1994, ApJ, 436, 11
- Athanassoula, E. 2002a, The Dynamics, Structure, & History of Galaxies: A Workshop in Honour of Professor Ken Freeman, ASP Conference Proceedings, Vol 273. Edited by G. S. Da Costa and Helmut Jerjen, 85
- Athanassoula, E. 2002, ApJ, 569, L83
- Athanassoula, E., & Misiriotis, A. 2002, MNRAS, 330, 35
- Athanassoula, E. 2003, in press [astro/ph-0302519]
- Avila-Reese, V., Colín, P., Valenzuela, O., D'Onghia, E., & Firmani, C. 2001, ApJ, 559, 516
- Barnes, J. 1998, Dynamics of Galaxy Interactions, Galaxies: Interactions and Induced Star Formations, Saas-Fee Advanced Course 26. eds. R.C. Kennicutt, Jr., F. Schweizer, J. E. Barnes, D. Friedli, L. Martinet, and D. Pfenniger, p275
- Barnes, J., & Hernquist, L. 1992, ARA&A, 30, 705
- Barnes, J. 1992, ApJ, 393, 484
- Barnes, J., & White, S. D. M. 1984, MNRAS, 211, 753
- Binney, J. & Tremaine, S. 1987, Galactic Dynamics, Princeton University Press
- Binney, J., Gerhard, O., & Silk, J. 2001, MNRAS, 321, 471
- Blumethal, G. R., Faber, S. M., Flores, R., & Primack, J. R. 1986, ApJ, 301, 27
- Bode, P., Ostriker, J. P., & Turok, N. 2001, ApJ, 556, 93
- Bottema, R., & Gerritsen, J. P. E. 1998, MNRAS, 290, 585
- Bottema, R. 1997, A&A, 328, 517
- Brown, M. J. W., & Papaloizou, J. C. B. 1998, MNRAS, 300, 135
- Bullock, J.S., Kolatt, T.S., Sigad, Y., Somerville, R.S., Kravtsov, A.V., Klypin, A.A., Primack, J.R., Dekel, A. 2001, MNRAS, 321, 559
- Cen, R. 2001, ApJ, 546, L77
- Clutton-Brock, M. 1972, A&A, 16, 101
- Clutton-Brock, M. 1973, A&A, 23, 55
- Colín, P., Avila-Reese, V., & Valenzuela, O. 2000, ApJ, 542, 622
- Côté, S. 1997, ASP Conf. Ser. 117: Dark and Visible Matter in Galaxies and Cosmological Implications, ed. M. Persic & P. Salucci (San Francisco: ASP), 52
- Côté, S., Carignan, C., & Freeman, K. 2000, AJ, 120, 3027
- Courant, R., & Hilbert, D. 1953, Methods of Mathematical Physics, Vol. 1 (New York: Interscience)
- Debattista, V., & Sellwood, J. A. 1998, ApJ, 493, L5
- Debattista, V., & Sellwood, J. A. 2000, ApJ, 543, 704
- Debattista, V. P., & Williams, T. B. 2001, gddg.conf, 553
- Dehnen, W. 2001, MNRAS, 324, 273
- Dehnen, W. 2002, in press, [astro-ph/0202512]
- de Blok, W. J. G., McGaugh, S., Bosma, A., & Rubin, V. 2001, ApJ, 552, L23
- de Blok, W. J. G., & Bosma, A. 2002, A&A, 385, 816
- de Blok, W. J. G., McGaugh, S., & Rubin, V. 2001, AJ, 122, 2396
- Dubinski, J. 1994, ApJ, 431, 617
- Earn, D. J. D. 1996, ApJ, 465, 91
- Earn, D. J. D., & Sellwood, J. A. 1995, ApJ, 451, 533
- Elmegreen, B., Elmegreen, D., Chromey, F., Haselbacher, D., Bissell, B. 1996, AJ, 111, 2233
- El-Zant, A., Shlosman, I., & Hoffman, Y. 2001, ApJ, 560, 636
- El-Zant, A., & Shlosman, I. 2002, ApJ, 577, 626
- Friedli, D., & Benz, W. 1993, A&A, 268, 65
- Friedman, A. L., & Polyachenko, V. L. 1984, Physics of Gravitating Systems, Vol. 2 (New York: Springer), 282
- Fall, S. M., & Efstathiou, G., 1980, MNRAS, 198, 189

- Font, A. S., Navarro, J. F., Stadel., & Quinn, T. 2001, *ApJ*, 563, L1
- Gnedin, N., N. Y., & Bertschinger, E. 1996, *ApJ*, 470, 115
- Gnedin, O., & Zhao, H. 2002, *MNRAS*, 333, 299
- Goodman, J. 2000, *New Astronomy*, 5, 103
- Gondolo, P., & Silk, J. 1999, *Phys. Rev. D*, 83, 9, L1719
- Hall, A. N. 1981, *Ann. Stat.*, 9, 683
- Hasan, H, & Norman, C. 1990, *ApJ*, 361, 69
- Hernquist, L., 1990, *ApJ*, 356, 359
- Hernquist, L., 1993, *ApJS*, 86, 389
- Hernquist, L., & Barnes, J. 1990, *ApJ*, 349, 562
- Hernquist, L., & Ostriker, J. P. 1992, *ApJ*, 386, 375
- Hernquist, L., Sigurdsson, S., & Bryan, G. L. 1995, *ApJ*, 446, 717
- Hernquist, L., & Weinberg, M. 1992, *ApJ*, 400, 80
- Hogan, C., & Dalcanton, J. 2000, *Phys. Rev. D*, D62, 817
- Jessop, C., Duncan, M., & Chau, W. Y. 1994, *Journal of Computational Physics*, 115, 339
- Jesseit, R., Naab, T., & Burkert, A. 2002, *ApJ*, L89
- Jing, Y.P. 2000, *ApJ*, 535, 30
- Jogee, S., Knapen, J., Laine, S., Shlosman, I., Scoville, N., & Englmaier, P. 2002, *ApJ*, 570, L55
- Kalnajs, A. J. 1976, *ApJ*, 205, 745
- Kamionkowski, M., & Liddle, A. 2000, *Phys. Rev. Lett.*, 84, 4525
- Kandrup, H., & Sideris, I. 2003, *ApJ*, 585, 244
- Kaplinghat, M., Knox, L., & Turner, M. 2000, *Phys. Rev. Lett.*, 85, 3335
- Kolatt, T.S., Bullock, J., Sigad, Y., Kravtsov, A.V., Klypin, A.A., Primack, J.R., & Dekel, A. 2000, in press. [astro-ph/0010222]
- Kravtsov, A., Klypin, A., & Khokhlov, A. 1997, *ApJS*, 111, 73
- Lacey, C. G., & Ostriker, J. P. 1987, *IAU Circ.*, 117, 412
- Lokas, E., & Mamon, G. 2001, *MNRAS*, 321, 155
- Lynden-Bell, D. & Kalnajs, A. 1972, *MNRAS*, 157, 1
- Makino, J. 1997, *ApJ*, 478, 58
- McGaugh, S. 2002, *The Shapes of Galaxies and Their Dark Halos*, Proceedings of the Yale Workshop “The Shapes of Galaxies and Their Dark Halos”, Edited by Priyamvada Natarajan, 186
- Merrifield, M., & Kuijken, K. 1995, *MNRAS*, 274, 933
- Milosavljevic, M., Merritt, D., Rest, A., & van den Bosch, F. 2002, *MNRAS*, 331, 51
- Moore, B., Quinn, T., Governato, F., Stadel, & Lake, G. 1999a, *MNRAS*, 310, 1147
- Moore, B., Ghigna, S., Governato, F., Lake, G., Quinn, T., Stadel, J., & Tozzi, P. 1999b, *ApJ*, 524, L19
- Navarro, J., Frenk, C., & White, S. D. M. 1996, *ApJ*, 462, 563
- Navarro, J., Eke, V., & Frenk, C. 1996, *MNRAS*, 283, 72
- Noguchi, M. 1996, *Barred Galaxies*, *IAU Circ.*, 157, 339
- Noguchi, M. 1988, *A&A*, 203, 289
- Ostriker, J., & Peebles, P. J. E. 1973, *ApJ*, 186, 467
- Peebles, P. J. E. 2000, *ApJ*, 534, L127
- Persic, M., Salucci, P., & Stel, F. 1996, *MNRAS*, 281, 27
- Pfenniger, D. 1991, *Dynamics of Disc Galaxies: Varberg Castle Sweden*, 191
- Polyachenko, V. L., & Polyachenko, E.V. 1996, *Astonomy Letters*, 22, 302
- Polyachenko, V. L., & Shukhman, I. 1981, *AZh*, 58, 933 (English trans. in *Soviet Astron.*, 25, 533 [1981]) York: Oxford Univ. Press)
- Quillen, A.C., & Frogel, J. 1997, *ApJ*, 487, 603
- Saha, P. 1993, *MNRAS*, 262, 1062
- Salucci, P., & Burkert, A. 2000, *ApJ*, 537, L9
- Salucci, P. 2001, *MNRAS*, 320, L1
- Salucci, P. & Borriello, A., in press [astro-ph/0203457]
- Sellwood, J. A. 2002, in press, [astro-ph/0210079]

- Sellwood, J. A. 1996, *A.S.P.*, 91, 259
- Sheth, K., Vogel, S., Regan, M., Teuben, P., Harris, A., Thornley, M. 2002, *AJ*, 124, 2581
- Sheth, K., Regan, M., Scoville, N., & Strubbe, L. 2003, *ApJ*, in press [astro-ph/0305589]
- Somerville, R.S., Primack, J.R., & Faber, S.M. 2001, *MNRAS*, 320, 504
- Spiegel, D. N. & Steinhardt, P. J. 2000, *Phys. Rev. Lett.*, 84, 3760
- Steinmetz, M., & Navarro, J. 2002, *New Astronomy*, 7, 155
- Toomre, A., *ApJ*, 139, 1217
- Tóth, G., & Ostriker, J. P. 1992, *ApJ*, 389, 5
- Ullio, P., Bergstrom, L., Edsjo, J., Lacey, C. 2002, *Phys. Rev. D*, 66, 12, 123502
- Tremaine, S., & Weinberg, M. 1984, *MNRAS*, 209, 729
- Valenzuela, O., & Klypin, A. 2002, *MNRAS*, in press [astro-ph/0204028]
- van Albada T.S & Sanders, R. H. 1982, *MNRAS*, 201, 303
- van den Bergh, S., Abraham, R., Whyte, L., Merrifield, M., Eskridge, P., Frogel, J., Pogge, R. 2002, *AJ*, 123, 2913
- Walker, I., Mihos, C., & Hernquist, L. 1996, *ApJ*, 460, 121
- Weinberg, M. 1996, *ApJ*, 470, 715
- Weinberg, M. 1999, *AJ*, 117, 629
- Weinberg, M., & Katz, N. 2002, *ApJ*, 580, 627
- Weinberg, M., 2001, [astro-ph/0101296]
- Weinberg, M., 2001, *MNRAS*, 328, 321
- Weinberg, M., & Katz, N. 2003, *ApJ*, in press